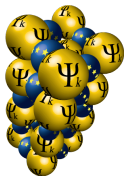

Ψ_k **Scientific Highlight Of The Month**

No. 150 **November 2020**

Correlated Delafossites: from Basic Properties to Mott Design

Frank Lechermann[1,*]

[1] *European XFEL, Holzkoppel 4, 22869 Schenefeld, Germany*

Abstract

The natural-heterostructure concept realized in delafossites designates these oxides from other layered compounds. While metallic, band- or Mott-insulating character may be associated with individual layers in selected delafossite materials, the inter-layer coupling still plays a decisive role. We here review the correlated electronic structure of $PdCoO_2$, $PdCrO_2$ and $AgCrO_2$, and show that the layer-entangled electronic states may easily deviate from standard classifications of interacting electron systems. This does not only render the investigation of the bulk systems highly interesting, but additionally opens up possibilities for materials design in a subtle Mott-critical regime. Therefore, engineering options that further enrich the fascinating delafossite phenomenology are discussed on a theoretical level. Hidden-Mott physics, correlation-induced semimetallicity, or Dirac/flat-band dispersions in a Mott background are only a few demanding features that may emerge in delafossite physics. Together with novel achievements in the experimental preparation of such materials, this may inaugurate a new exciting research field in the arena of correlated materials.

*frank.lechermann@xfel.eu

Contents

1 Introduction

When it comes to the research on strongly correlated materials, and especially from a theory perspective, a common statement refers to the fact that the body of compounds that fall into this category is rather small, and hence the relevance and impact in general materials science scales accordingly. While there has been some truth in this view, there are also obvious facts that argue against. First undoubtedly, the properties of various correlated systems are singular. High-temperature superconductivity in cuprates or colossal magnetoresistance in manganites are only two extraordinary features that stand out in condensed matter physics. Moreover, even 'straightforward' materials properties, such as e.g. magnetism in the solid state, are often relying on some effect of electronic correlation. Second, times are changing and from a technological applicative viewpoint, understanding and engineering electron correlation may be indispensable to make progress in battery materials, thermoelectric devices, photovoltaic systems, data-storage media or other sorts of 'smart' materials. Against this background, we want to discuss in this overview the fascinating physics of a certain class of transition-metal (TM) oxides prone to correlation effects, namely the *delafossites*. Importantly, this materials class is not only of

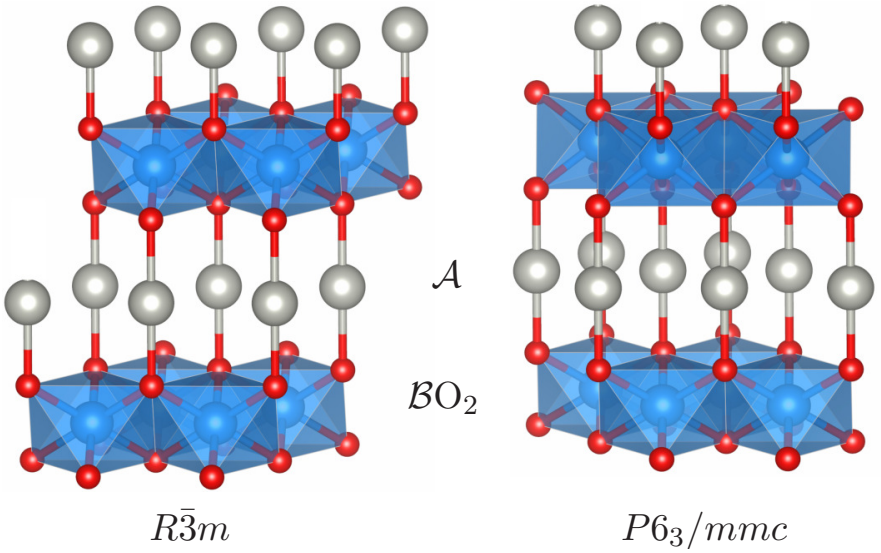

Figure 1: Delafossite $\mathcal{A}\mathcal{B}O_2$ crystal structure with (left) $R\bar{3}m$ and (right) $P6_3/mmc$ symmetry: $\mathcal{A}$ (grey), $\mathcal{B}$ (blue) and O (red).

interest due to its intrinsic basic properties, but also because of the potential for even more intriguing characteristics upon further design.

Delafossites, named after the french crystallographer Gabriel Delafosse (1796-1878), are in fact known for quite some time. The first delafossite, the $CuFeO_2$ mineral, has been discovered [1] near Yekaterinburg, Russia in 1873 and then re-discovered [2] near Bisbee(Arizona), USA in 1913. Since then, numerous compounds of the delafossite-oxide type $\mathcal{A}\mathcal{B}O_2$, where $\mathcal{A}$ and $\mathcal{B}$ denote different metallic elements, have been crystallized. The unique crystal structure (see Fig. 1) consists of an alternate stacking of triangular $\mathcal{A}$ lattices and planes of edge-sharing $\mathcal{B}O_6$ octahedra along the c-axis, whereby these two different layer types are connected via oxygen in a so-called dumbbell position. There are two possible stacking scenarios, namely the more common rhombohedral one with $R\bar{3}m$ space-group symmetry and the hexagonal one giving rise to $P6_3/mmc$ symmetry. The metallic ions are in the formal oxidation state $\mathcal{A}^+$ and $\mathcal{B}^{3+}$, respectively.

Delafossites are divided into a larger insulating and a smaller metallic class of compounds. In modern times, the p-type electrical conduction in the transparent $CuAlO_2$ insulator [3] gained strong interest. In a series of papers [4–6], Shannon *et al.* in 1971 described the novel synthesis and single-crystal growth of several delafossites with $\mathcal{A}$=Pd, Pt and Ag. Among those, there are oxides with exceptionally high electrical conductivity at room temperature, e.g. $PdCoO_2$ and $PtCoO_2$, in combination with an outstanding single-crystal purity. This combined feature found in a selected subgroup of delafossites has started to become an intense field of research in recent years (see e.g. Refs. [7, 8] for reviews). This elitist group of delafossites in terms of metallic properties, includes the $PdCrO_2$ compound, which, among further challenging physics, hosts Mott-insulating CrO_2 layers [9–11].

This brings us to a further very relevant aspect of delafossites. Their special architecture

gives rise to a natural heterostructure, in which individual layers may attain a distinct character of their own. In most layered materials, e.g. cuprates, cobaltates, etc., there is usually one 'active' layer type and the remaining part mainly provides the glue to hold everything together. However in delafossites, e.g. the $\mathcal{A}$ layer can manage the metallic transport, while the $\mathcal{B}O_2$ layers account for the magnetic ordering. This not only entails exciting physical processes in the pure compound, but furthermore allows for a kind of 'meta oxide-heterostructure' physics upon additional (nano-)engineering.

In order to theoretically investigate such challenging systems with subtle electronic characteristics, an advanced framework is needed, capable of addressing electron states from weak to strong correlation on an equal footing. Model-Hamiltonian approaches may only be used at a later stage, when focussing on certain details of the complex quantum problem. Density functional theory (DFT) in Kohn-Sham representation is proper to describe the band formation from first principles, but will not be sufficient to account for relevant correlation effects. The combination of DFT with dynamical mean-field theory (DMFT), the so-called DFT+DMFT method [12–14], is well suited for the problem, as it can account for site- and orbital-resolved Mott criticality at strong coupling as well as for mildly renormalized dispersions at weak coupling in a realistic setting.

Since the family of delafossites encircles a vast number of compounds with many different physical aspects, we cannot reasonably-well cover all those in this comparatively brief treatise. Instead, the goal is to focus on the specific role of electron correlations in selected compounds with A=Pd, Ag and $\mathcal{B}$=Co, Cr as well as an assessment of possible designing routes. For further discussion of delafossites we refer the reader to the exisiting body of literature, e.g. Refs. [7, 8, 15–17] and references therein.

Before delving into the details of the correlated electronic structure of delafossites, a reminder of the state-of-the-art DFT+DMFT approach is first given in the next section 2. Since this review is intended to focus on the materials and the correlation-design aspect, that theory part will be rather brief. There are already various more extensive descriptions of DFT+DMFT, e.g. [18–20].

2 Density functional theory plus dynamical mean-field theory

2.1 General formalism

Describing the general many-body problem from weak to strong coupling in a condensed matter system within a first-principles(-like) manner is tough. A unique and well-defined solution has not been given yet. Especially when one also wants to address materials science questions with larger unit cells and larger orbital manifolds, a solution presumably has to wait for much longer times. Approximate hybrid methods that divide the complex problem into (coupled) subproblems of different significance have proven adequate to obtain good results beyond effective single-particle schemes. The DFT+DMFT technique is such a hybrid method.

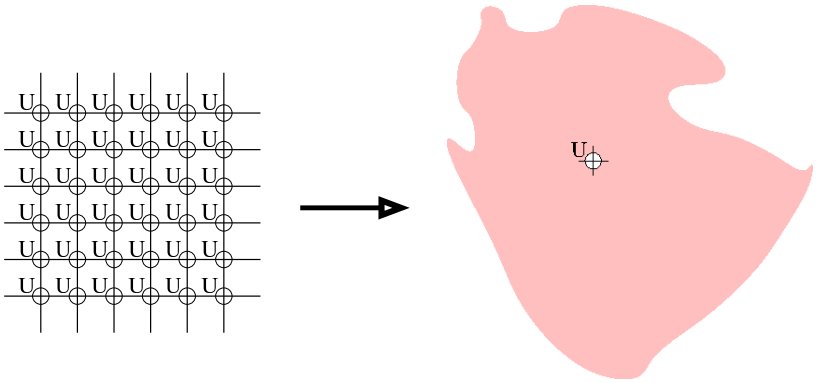

Figure 2: Sketch of the basic DMFT mapping. An interacting electron system on a lattice with a Coulomb repulsion U on each site is mapped onto a single interacting site in an energy-dependent bath. The latter is determined self-consistently in an iterative cycle.

We assume that the reader is familiar with DFT[1], so let us spend a few words on DMFT. The dynamical mean-field theory [21, 22] was invented for model Hamiltonians and is appreciated as the many-body scheme with the best compromise between generality, accuracy and performance. Just as Kohn-Sham DFT, also DMFT describes a mapping: from the problem of interacting lattice electrons onto the problem of a quantum impurity within a self-consistent energy-dependent bath, sketched in Fig. 2. Key focus is on the one-particle Green's function, which for chemical potential μ and Hamiltonian $H(\mathbf{k})$ at wave vector $\mathbf{k}$ reads

$$G(\mathbf{k}, i\omega_\mathrm{n}) = [i\omega_\mathrm{n} + \mu - H(\mathbf{k}) - \Sigma(\mathbf{k}, i\omega_\mathrm{n})]^{-1} \quad . \tag{1}$$

Note that here, fermionic Matsubara frequencies $\omega_\mathrm{n} := (2n+1)\pi T$ are employed to emphasize the treatment at *finite* temperature. The analytical continuation to real frequencies ω in actual calculations may e.g. be performed via the maximum entropy method (see e.g. [23, 24] for more details). The self-energy Σ describes the many-body part of the problem, and hence, finding a good approximation is key to a physically sound picture. In DFT, the self-energy is approximated, in essence, by the energy-independent sum of Hartree potential v_H and exchange-correlation potential v_{xc} in the form of a simple forward-scattering term. In DMFT, the local Green's function is approximated with the help of a $\mathbf{k}$-independent but energy-dependent impurity self-energy $\Sigma_\mathrm{imp}(i\omega_\mathrm{n})$, i.e.

$$G_\mathrm{loc}^\mathrm{DMFT}(i\omega_\mathrm{n}) = \sum_\mathbf{k} [i\omega_\mathrm{n} + \mu - H(\mathbf{k}) - \Sigma_\mathrm{imp}(i\omega_\mathrm{n})]^{-1} \quad , \tag{2}$$

whereby the corresponding impurity problem is defined via

$$\Sigma_\mathrm{imp}(i\omega_\mathrm{n}) = \mathcal{G}_0(i\omega_\mathrm{n})^{-1} - G_\mathrm{imp}(i\omega_\mathrm{n})^{-1} \quad . \tag{3}$$

[1]The term 'DFT' is understood throughtout the text as 'effective single-particle Kohn-Sham DFT'. While this discrimination is important, we here focus on practical calculations and shorten the abbrevation for readability matters.

The Weiss field $\mathcal{G}_0(i\omega_\mathrm{n})$ is a function of the local Hamiltonian (expressed within a localized basis). The important DMFT self-consistency condition implies $G_\mathrm{imp} = G_\mathrm{loc}^\mathrm{DMFT}$ and is usually achieved within a loop, just as the Kohn-Sham cycle. From an initial version of $\mathcal{G}_0$, the self-energy Σ_imp is determined and with the use of (2),(3) a new $\mathcal{G}_0$ extracted, and so on. The hard part consists in solving the quantum-impurity problem to obtain G_imp for a given Weiss field. So-called 'solvers' based e.g., on quantum Monte Carlo, Exact Diagonalization, etc. are employed for that task. Note that local-interaction diagrams are included to all orders in this non-perturbative theory. The vital energy dependence of the Weiss field ensures the qualitatively correct description of low-energy quasiparticle (QP) features as well as high-energy incoherent (Hubbard) excitations. Extensions to overcome the restriction to a local self-energy, e.g. via cluster schemes, are available, but will not be pursued here.

We now come back to the portioning into subspaces within DFT+DMFT. Concerning DFT for a few hundred sites, there is no issue for conventional exchange-correlation functionals and one may apply that approach to the complete electronic Hilbert space. This ensures a reliable description of the bonding, band formation and screening properties in a given material. On the other hand, DMFT as a manifest many-body scheme is not applicable to hundreds of sites. Furthermore and very importantly, there are further issues to the use of pure DMFT in a concrete materials context. First, DMFT builds up on the physics of interactions in orbitals with reasonably local character, i.e. a Hubbard-model-like scenario. However, such a scenario is not straightforwardly suitable for e.g. dominant s and p electron states. Second, DMFT is designed to provide proper access to the self-energy Σ, but not to derive general hoppings t. In other words, a full-monty DMFT starting from atomic Coulomb potentials on a given lattice is just not the conventional modus operandi. Note that there are ideas to use DMFT for quantum chemistry problems in a direct manner [25, 26], but it is still a long way to condensed matter materials science. Therefore, putting materials-oriented DMFT into practise is currently best done by allocating a restricted Hilbert subspace, i.e. the so-called *correlated subspace*.

The correlated subspace is understood as a quantum-numbered real-space region where correlated electrons reside. Note that this subspace is not uniquely defined, but is a matter of choice in a concrete materials problem. For instance, in the case of an early transition-metal oxide, like e.g. $SrVO_3$ or V_2O_3, it may consist of the low-energy t_{2g} orbitals of the TM site(s). Within the correlated subspace, a multi-orbital interacting Hamiltonian is applied to the orbitals. More concretely, the corresponding Hamiltonian terms are explicitly exploited in the impurity solver. The Hamiltonian is usually of generalized Hubbard type, with local interaction parameters based on the Coulumb integral U and the Hund exchange J_H. Those are either chosen by hand or computed ab-initio, e.g via the constrained random-phase approximation [27].

Key interfaces of the complete DFT+DMFT self-consistency cycle [28–31] (cf. Fig. 3) are marked by the downfolding of the full-problem Bloch space to the correlated subspace, and the upfolding of the DMFT self-energy back to the full space. In terms of the Green's function G and the self-energy Σ, for sites $\mathbf{R}$, local orbitals mm' and band indices $\nu\nu'$ this reads formula-wise

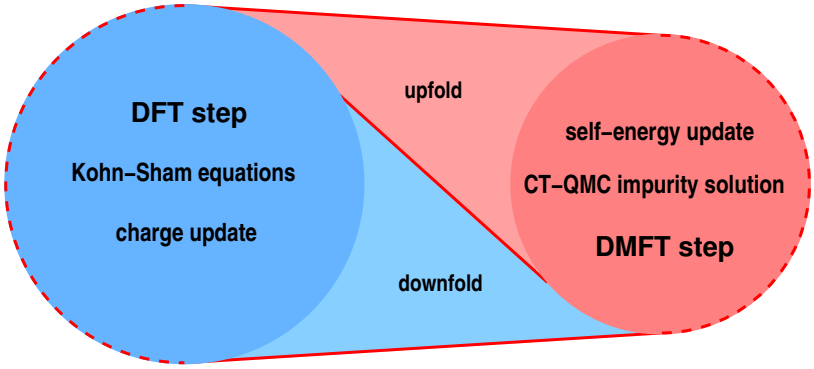

Figure 3: State-of-the-art charge self-consistent DFT+DMFT loop (after [32]). The calculation usually starts from a self-consistent Kohn-Sham solution. The correlated subspace is defined and the initial Weiss field $\mathcal{G}_0$ constructed. Afterwards, a single DMFT step is performed. The obtained self-energies are upfolded and an updated charge density $n(\mathbf{r})$ is computed. A new charge density implies a new Kohn-Sham potential, and a single new Kohn-Sham step is performed, therefrom a new Weiss field is generated, etc..

$$G^{\mathbf{R},\mathrm{imp}}_{mm'}(i\omega_\mathrm{n}) = \sum_{\mathbf{k},(\nu\nu')\in\mathcal{W}} \bar{P}^{\mathbf{R}}_{m\nu}(\mathbf{k})\, G^{\mathrm{bloch}}_{\nu\nu'}(\mathbf{k}, i\omega_\mathrm{n})\, \bar{P}^{\mathbf{R}*}_{\nu' m'}(\mathbf{k}) \quad , \tag{4}$$

$$\Delta\Sigma^{\mathrm{bloch}}_{\nu\nu'}(\mathbf{k}, i\omega_\mathrm{n}) = \sum_{\mathbf{R},mm'} \bar{P}^{\mathbf{R}*}_{\nu m}(\mathbf{k})\, \Delta\Sigma^{\mathbf{R},\mathrm{imp}}_{mm'}(i\omega_\mathrm{n})\, \bar{P}^{\mathbf{R}}_{m'\nu'}(\mathbf{k}) \quad , \tag{5}$$

with $\bar{P}$ denoting the normalized projection between Bloch space and correlated subspace [33]. Note that eq. (4) is necessary to define the notion of a local Green's function (eq. (2)) for the DMFT problem. As for the correlated subspace, there is a choice for the range $\mathcal{W}$ of included Kohn-Sham bands in the downfolding. The object $\Delta\Sigma^{\mathrm{bloch}}_{\nu\nu'}$ describes the $\mathbf{k}$-dependent self-energy in Bloch space after a double-counting correction. The latter takes care of the fact that some correlations are already handled on the DFT level. In the upfolding operation, the charge density $n(\mathbf{r})$ is then decorated with DMFT correlations, i.e.

$$n(\mathbf{r}) = \sum_{\mathbf{k},\nu\nu'} \langle\mathbf{r}|\Psi_{\mathbf{k}\nu}\rangle \Big(f(\tilde{\epsilon}_{\mathbf{k}\nu})\delta_{\nu\nu'} + \Delta N_{\nu\nu'}(\mathbf{k}) \Big) \langle\Psi_{\mathbf{k}\nu'}|\mathbf{r}\rangle \quad , \tag{6}$$

where Ψ denotes Kohn-Sham states, f marks the associated Fermi function and ΔN refers to the DMFT Bloch-density term [32, 33]. A pure band picture is not adequate for a many-body system and *real-space* excitations also matter. Therefore, additional off-diagonal terms in the band index contribute in the correlated regime. This extended charge-density formulation accordingly then defines a new Kohn-Sham potential. Let us finally iterate on the fact that this realistic many-body scheme works, at heart, at finite temperature T. Electron states are subject to the full thermal impact, beyond sole occupational Fermi-function modification. For more formal accounts on the DFT+DMFT scheme, we refer to [14, 18].

In various problems of multi-atom unit cells, the correlated subspace encircles not only a single lattice site. For symmetry-equivalent sites, the self-energy is determined for a representative site and transferred to the remaining sites via proper symmetry relations. An impurity

problem is defined for each symmetry-inequivalent site j through [34]

$$\mathcal{G}_0^{(j)}(i\omega_\mathrm{n})^{-1} = G^{(j)}(i\omega_\mathrm{n})^{-1} + \Sigma_\mathrm{imp}^{(j)}(i\omega_\mathrm{n}) \quad , \tag{7}$$

and the coupling is realized via the DFT+DMFT self-consistency condition invoking the computation of the complete lattice Green's function.

This concludes the brief sketch of the charge self-consistent DFT+DMFT methodology [28, 30, 31]. In the next subsection, we turn to the actually chosen representation to tackle delafossites.

2.2 Concrete setting for delafossites

Charge self-consistent DFT+DMFT is employed for all electronic structure problems discussed and addressed in this overview for $\mathcal{AB}O_2$-based delafossite. A mixed-basis pseudopotential method [35–37], based on norm-conserving pseudopotentials and a combined basis of localized functions and plane waves is used for the DFT part. The generalized-gradient approximation in form of the PBE functional [38] is utilized for the exchange-correlation functional. Within the mixed basis, localized functions for the transition-metal $3d$ and $4d$ shells, as well as for O($2s$,$2p$) are used to reduce the plane-wave energy cutoff. The latter is set to 20 Ryd for the bulk systems, and to 16 Ryd for the heterostructures. The k-point mesh amounts to 13×13×13 for the bulk and 11×11×3 (9×9×5) for out-of-plane(in-plane) heterostructures, respectively. For all systems, the experimental lattice parameters are adopted and the internal degree of freedom z, governing the oxygen distance to the $\mathcal{A}$ plane, is obtained from DFT structural optimization.

We choose the correlated subspace to be build up from the five effective $\mathcal{B}$-site Wannier-like $3d$ functions as obtained from the projected-local-orbital formalism [33, 40], using as projection functions the linear combinations of atomic $3d$ orbitals which diagonalize the $\mathcal{B}$-site $3d$ orbital-density matrix. As it will be seen later, the most-relevant correlated states in delafossites are of threefold t_{2g} kind. However due to the subtle hybridization between two different TM sites and our further designing perspective, we stick to the more general full $3d = \{t_{2g}, e_g\}$ fivefold throughout the presented results. For selected aspects, a reduction of the correlated subspace to the t_{2g} sector might still be an acceptable approximation.

A five-orbital Slater-Kanamori Hubbard Hamiltonian, i.e. including density-density, spin-flip and pair-hopping terms, is utilized in the correlated subspace, parametrized by a Hubbard

compound	a in Å	c in Å	z
$PdCoO_2$	2.830	17.743	0.1132
$PdCrO_2$	2.930	18.087	0.1101
$AgCrO_2$	2.985	18.510	0.1095

Table 1: Experimental lattice parameters [4–6, 39] of the studied bulk delafossites, as well as the DFT optimized internal z degree of freedom.

U and a Hund exchange J_{H}. It reads for orbitals m, m'

$$H_{\mathrm{int}} = U \sum_{m} n_{m\uparrow} n_{m\downarrow} + \frac{1}{2} \sum_{m \neq m', \sigma} \Big\{ (U - 2J_{\mathrm{H}})\, n_{m\sigma} n_{m'\bar{\sigma}} + (U - 3J_{\mathrm{H}})\, n_{m\sigma} n_{m'\sigma} + \\ + J_{\mathrm{H}} \left(c^{\dagger}_{m\sigma} c^{\dagger}_{m'\bar{\sigma}} c_{m\bar{\sigma}} c_{m'\sigma} + c^{\dagger}_{m\sigma} c^{\dagger}_{m\bar{\sigma}} c_{m'\bar{\sigma}} c_{m'\sigma} \right) \Big\} \ , \tag{8}$$

with $c^{(\dagger)}_{m\sigma}$ as the annihilation(creation) operator for spin flavor $\sigma = \uparrow, \downarrow$, and $n = c^{\dagger} c$. Our $\mathcal{B}$ site will here be either of Co or Cr type and a value of $J_{\mathrm{H}} = 0.7\,\mathrm{eV}$ is proper for TM oxides of that kind. Hubbard U values between $3-4\,\mathrm{eV}$ will be chosen according to adequate onsite Coulomb integrals for similiar types of oxides [41,42]. Note that no further Hubbard interactions are assigned to the $\mathcal{A}$ site. The d orbitals on those sites will be here of $4d$ kind, of formal d^9 filling and only weakly hybridizing with oxygen. Thus by any means, Coulomb interactions are expected much smaller than on the $\mathcal{B}$ site. Spin-orbit coupling is neglected in the calculations.

The encountered DMFT impurity problems in the examined delafossite materials are solved by the continuous-time quantum Monte Carlo scheme of hybridization-expansion form [43,44] as implemented in the TRIQS package [45,46]. A double-counting correction of fully-localized-limit type [47] is applied in all calculations. To obtain the spectral information, analytical continuation from Matsubara space via the maximum-entropy method as well as the Padé method is performed. Though the $\mathcal{A}CrO_2$ delafossites order antiferromagnetically at low temperatures within the CrO_2 layers, our investigations remain at still higher temperatures and assume paramagnetism for all studied cases. If not otherwise stated, the system temperature is set to $T = 290\,\mathrm{K}$.

3 Basic properties of CoO_2-based and CrO_2-based delafossites

3.1 General considerations

The delafossites $PdCoO_2$, $PtCoO_2$ and $PdCrO_2$ are metals with surprisingly high conductivity (see e.g. Refs. [7,8] for recent reviews). With an in-plane resistivity of 2.6 $\mu\Omega$cm [48], the $PdCoO_2$ compound is designated as the most-conductive oxide at room temperature. It apparently shows hydrodynamic flow of electrons [49]. Although obviously also a correlation effect [50], this feature will not be directly addressed in the present text, but further information can be found in Refs. [51–53] and references therein. The $AgCrO_2$ delafossite is an insulator with a charge gap of $\Delta = 1.68\,\mathrm{eV}$ [39]. While no ordering transition takes place in the Co compounds down to lowest

compound	$\varepsilon^{\mathcal{A}}_{a_{1g}}$	$\varepsilon^{\mathcal{A}}_{e'_g}$	$\varepsilon^{\mathcal{A}}_{e_g}$	$\varepsilon^{\mathcal{B}}_{a_{1g}}$	$\varepsilon^{\mathcal{B}}_{e'_g}$	$\varepsilon^{\mathcal{B}}_{e_g}$	a	b
$PdCoO_2$	-1082	-2177	-1953	-1320	-1415	-465	0.621	0.784
$PdCrO_2$	-969	-2057	-1847	-336	-493	831	0.586	0.810
$AgCrO_2$	-3195	-4139	-4080	-249	-459	743	0.548	0.837

Table 2: DFT Crystal-field levels on $\mathcal{A}$ and $\mathcal{B}$ site in the investigated delafossites, as well as orbital coefficients a, b on the $\mathcal{B}$ site. All energies in meV.

temperatures, the Cr compounds display magnetic transitions into an antiferromagnetic (AFM) 120° phase below the Néel temperatures 37.5 K ($PdCrO_2$) [54] and 21 K ($AgCrO_2$) [55, 56].

From symmetry, the local electronic d-shell states on $\mathcal{A}$ and $\mathcal{B}$ sites show a trigonal splitting into $t_{2g} = \{a_{1g}, e'_g\}$ and e_g classes (see also Ref. [57]). The e'_g and e_g states are doubly degenerate, respectively. The symmetry-adapted orbitals $|m_{\mathcal{A},\mathcal{B}}\rangle$ may be expressed as linear combinations of the atomic d orbitals. On the $\mathcal{A}$ site, there is a one-to-one matching between crystal-field orbitals and atomic orbitals, i.e. $|a_{1g}\rangle = |d_{z^2}\rangle$, $\left|e'_g(1,2)\right\rangle = |d_{xz}, d_{yz}\rangle$, $|e_g(1,2)\rangle = \left|d_{xy}, d_{x^2-y^2}\right\rangle$. On the $\mathcal{B}$ site, the identification is based on the usual trigonal representation, reading

$$\begin{pmatrix} |a_{1g}\rangle \\ \left|e'_g(1)\right\rangle \\ \left|e'_g(2)\right\rangle \\ |e_g(1)\rangle \\ |e_g(2)\rangle \end{pmatrix} = \begin{pmatrix} 1 & 0 & 0 & 0 & 0 \\ 0 & a & 0 & b & 0 \\ 0 & 0 & -a & 0 & b \\ 0 & 0 & b & 0 & a \\ 0 & b & 0 & -a & 0 \end{pmatrix} \begin{pmatrix} |d_{z^2}\rangle \\ |d_{xz}\rangle \\ |d_{yz}\rangle \\ |d_{xy}\rangle \\ \left|d_{x^2-y^2}\right\rangle \end{pmatrix} . \tag{9}$$

The values a, b may be obtained from diagonalizing the DFT orbital density matrix for the respective $3d$ shell after convergence of the crystal calculation. The nominal $\mathcal{B}^{3+}$ ion is usually in a low-spin configuration with its e_g states higher in energy and mostly empty. The collected DFT crystal-field levels of the d states on the respective $\mathcal{A}$ and $\mathcal{B}$ sites, along with the a, b coeffcients, are given in Tab. 2

Spin-orbit effects are assumed not to play a decisive role for the transport properties, however, they might have some influence in the magnetically ordered phases. The Co ion with configuration $Co^{3+}(3d^6)$ has a closed t_{2g} subshell in the local limit, which explains the absence of magnetic ordering in (Pd,Pt)CoO_2. On the other hand, $Cr^{3+}(3d^3)$ has a half-filled t_{2g} subshell in that limit. Therefore, correlation effects, which should predominantly originate from the TM($3d$) ions, are naturally expected stronger for (Pd,Ag)CrO_2. On the $\mathcal{A}$ sites, formally, the Pd ions have a $4d^9$ and the Ag ions a $4d^{10}$ oxidation state. Because of the filled Ag($4d$) shell and the insulating nature, the Cr electrons in $AgCrO_2$ are localized in a Mott fashion. Hence, $AgCrO_2$ is a combined 'band-Mott' insulator.

In the following, we will first discuss the more detailed electronic structure of $PdCoO_2$, $PdCrO_2$ and $AgCrO_2$ from a nonmagnetic Kohn-Sham DFT viewpoint. Previous DFT accounts of these system may be found e.g. in Ref. [9, 16, 57–62]. The respective impact of explicit electronic correlations within paramagnetic DFT+DMFT is elucidated in section 3.3.

3.2 DFT picture

For $PdCoO_2$, Fig. 4 displays the spectral DFT properties, namely density of states (DOS) and band structure of this metallic delafossite, as well as provides plots of the Wannier-like Pd($4d$) orbitals. As expected, the Pd($4d$) states are largely occupied with a bandwidth (W) hierachy of $W_{a_{1g}} > W_{e'_g} > W_{e_g}$. As shown in Fig. 4b, the Co($3d$) weight is mostly located in the bands close to and above the Fermi level $\varepsilon_{\rm F}$, with a single band crossing $\varepsilon_{\rm F}$. The latter dispersion, which we denote in the following 'cPd', is dominantly of mixed Pd($4d$) and partial Co($3d$) kind. In more detail from the Pd site, Pd-a_{1g} and Pd-e'_g have a comparable weight on the $\varepsilon_{\rm F}$-crossing regime of that most-relevant band. Note that the e'_g orbitals are the ones with the strongest

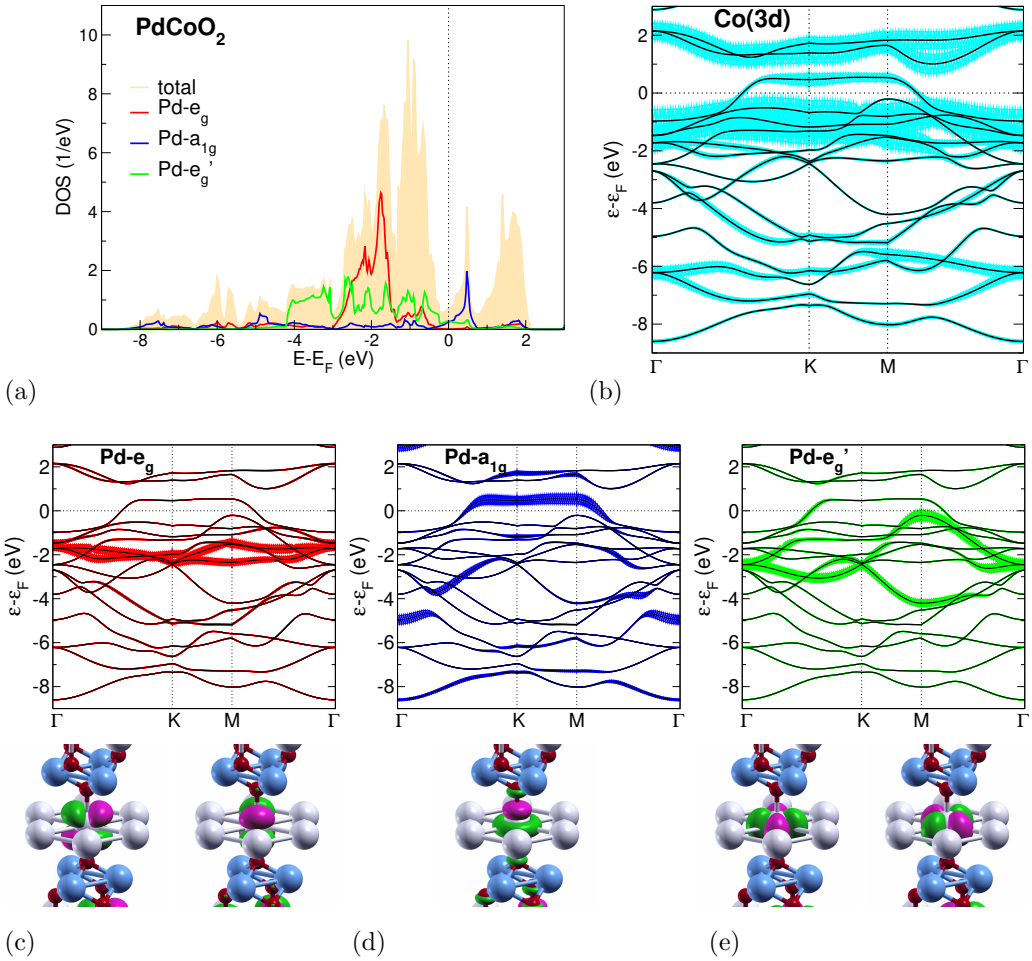

Figure 4: DFT electronic structure of $PdCoO_2$. (a) Total and orbital-resolved Pd($4d$) density of states. (b) Band structure along high symmetry lines in the $k_z = 0$ plane, with fatbands marking the Co($3d$) character. (c-d) Orbital resolved Pd($4d$) fatbands (top) and corresponding real-space Pd($4d$) projected local orbitals: Pd (grey), Cr (lightblue) and O (red).

in-plane character (see Fig. 4e). As a further note, though the band-filling Co($3d$) character resembles the original Co($3d^6$) picture, from the hybridizations at the Fermi level a completely inert Co-t_{2g} subshell is not truly justified. The DFT fermiology and dispersions at low energy are in good agreement with data from angle-resolved photoemission spectroscopy (ARPES) measurements [63] and de Haas-van Alphen studies [48]. Thus plain DFT seemingly provides already an adequate description of key $PdCoO_2$ features.

The spectral DFT properties of $PdCrO_2$ are shown in Fig. 5. Contrary to $PdCoO_2$, the $\mathcal{B}$-site states of Cr($3d$) character are much less filled, and the three t_{2g}-dominated bands are right at the Fermi level. On the other hand, the Pd($4d$) character at ε_F is minor. This low-energy picture of the dispersions however strongly disagrees with available experimental data from ARPES [9, 60] and quantum oscillations [64, 65]. In experiment, there is also only a single band crossing the Fermi level, quite similarly as in $PdCoO_2$. This discrepancy is due to the

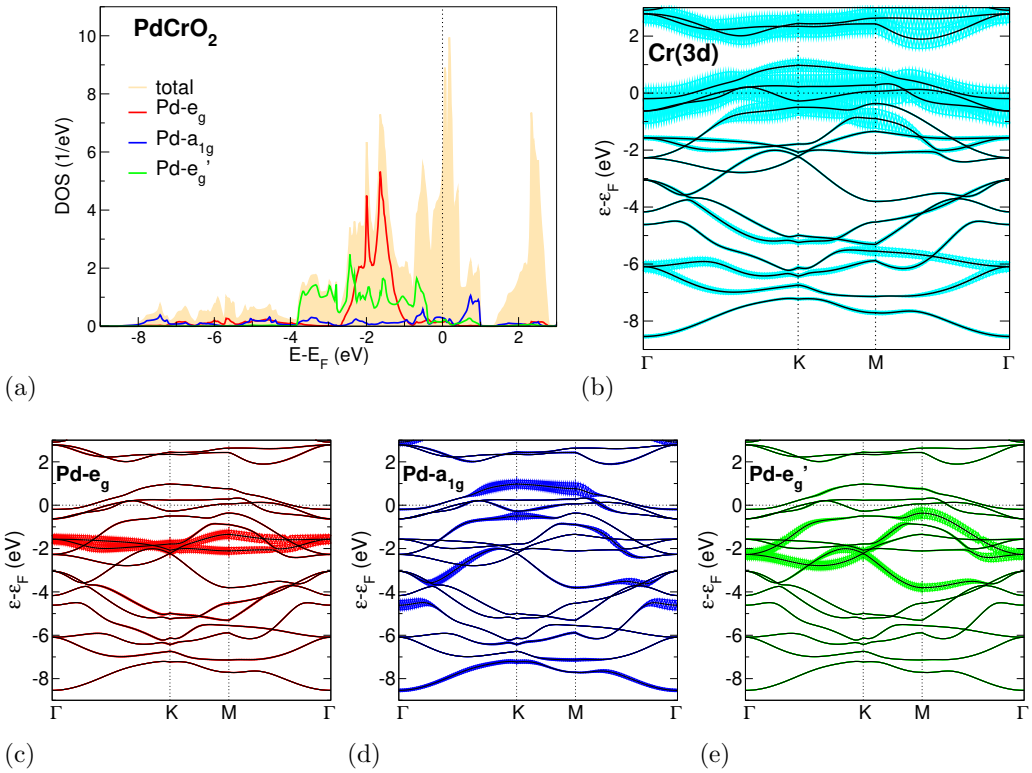

Figure 5: DFT electronic structure of $PdCrO_2$. (a) Total and orbital-resolved Pd($4d$) density of states. (b) Band structure along high symmetry lines in the $k_z = 0$ plane, with fatbands marking the Cr($3d$) character. (c-d) Orbital resolved Pd($4d$) fatbands.

neglect of strong electronic correlations in conventional DFT, which misses the Mott-localized character of the CrO_2 layers. Partial agreement with experiment concerning the dispersions can be achieved within spin-polarized DFT [9, 59, 60, 62], accounting also for the magnetic ordering at low temperatures. But this Slater-type handling of the Cr($3d$) states is not truly describing the underlying physics correctly. For instance, the single cPd dispersion holds for temperatures well above the magnetic-ordering temperature [60], therefore the gapping of Cr($3d$) is not linked to ordered magnetism.

Finally, the $AgCrO_2$ compound would be insulating in DFT if the Cr-t_{2g} states were not located again at the Fermi level (see Fig. 6). The Ag($4d$) states are filled and would give rise to a band insulator. The missing correlation effects on Cr become most evident in this delafossite. Note the prominent Pd-a_{1g} dominated band just below the Cr-t_{2g} bands in energy and with a nearly flat dispersion along K-M. It bears striking resemblance to the former low-energy cPd band in $PdCoO_2$. In fact as we will see in the following, this present band will just form the highest valence band in true $AgCrO_2$ once correlations are properly included. Furthermore for the same reason, the akin band in $PdCrO_2$ (yet there with stronger Pd-e'_g character) will be shifted to ε_F, giving rise to the experimentally revealed single-sheet fermiology.

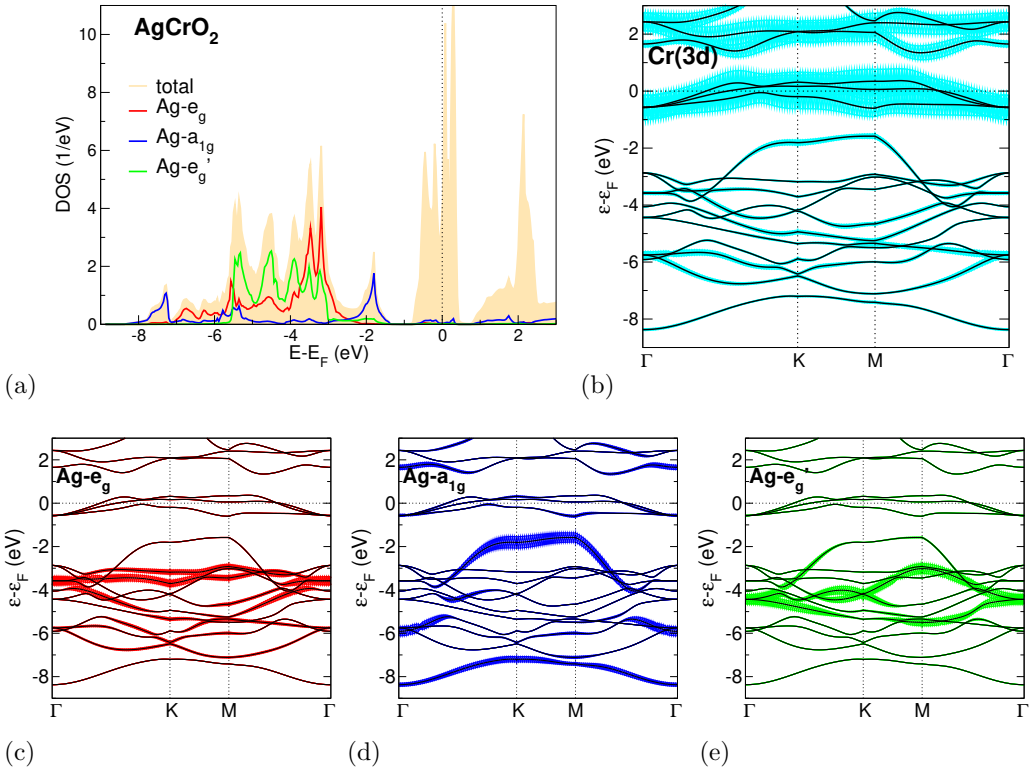

Figure 6: DFT electronic structure of $AgCrO_2$. (a) Total and orbital-resolved Ag($4d$) density of states. (b) Band structure along high symmetry lines in the $k_z = 0$ plane, with fatbands marking the Cr($3d$) character. (c-d) Orbital resolved Ag($4d$) fatbands.

3.3 DFT+DMFT picture

Let us now turn to the an improved description of the given delafossites, arising from the inclusion of correlation effects within DFT+DMFT. Concerning the Hubbard interaction, the value $U = 3\,\mathrm{eV}$ is assigned to the $3d$ states of Co and Cr in $PdCoO_2$ and $PdCrO_2$, respectively. For Cr($3d$) in $AgCrO_2$, the somewhat larger value of $U = 4\,\mathrm{eV}$ is used in order to comply with the weaker screening because of the (nearly) filled Ag($4d$) shell. A larger part of this subsection builds up on results and discussions provided in Refs. [10, 66].

3.3.1 Overview

Figure 7 exhibits the spectral summary for the three compounds. In the case of the Co compound, the changes compared to DFT appear minor, as already expected from the simplest picture of a closed Co-t_{2g} subshell. The dispersions, which now describe true quasiparticle features, are hardly modified at lower energy. Quite on the contrary, the QP dispersion for $PdCrO_2$ has changed dramatically (see Fig. 7b); the DFT-original Cr bands at ε_F have disappeared and instead, a single cPd dispersion as in $PdCoO_2$ crosses the Fermi level. This result brings theory eventually in line with experimental findings [9, 60, 64, 65]. Also for $AgCrO_2$, the DFT+DMFT approach settles the comparison with experiment, namely by identifying the insulating nature

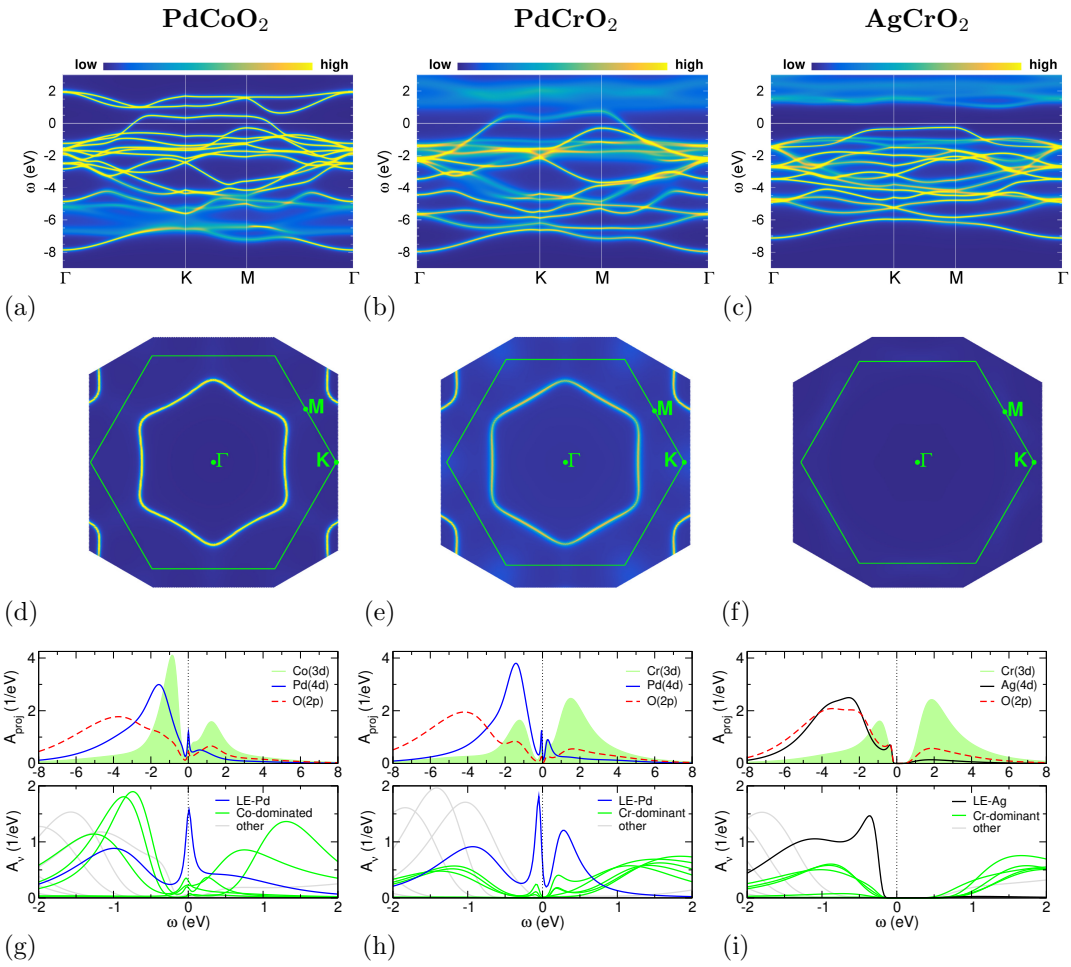

Figure 7: Spectral properties of $PdCoO_2$, $PdCrO_2$ and $AgCrO_2$ according to paramagnetic DFT+DMFT at $T = 290\,\mathrm{K}$. (a-c) $\mathbf{k}$-resolved spectral function $A(\mathbf{k}, \omega)$ along high symmetry lines in the $k_z = 0$ plane. (d-f) Interacting Fermi surface in the $k_z = 0$ plane. (g-h) Site- and orbital-rojected spectral function $A_{\mathrm{proj}}(\omega)$ (top) and Bloch-resolved spectral function $A_\nu(\omega)$, see text (bottom), respectively.

with a compatible gap of $\sim 1.8\,\mathrm{eV}$. While the latter delafossite shows of course no Fermi surface, the fermiology of $PdCoO_2$ and $PdCrO_2$ in Figs. 7d,e becomes rather similar with interactions. A single-sheet interacting Fermi surface, comprising a single electron, is centered around Γ and has a hexagonal shape with some warping. Note that this warping is somewhat stronger in the case of the Co compound.

Two functions are provided to discuss the $\mathbf{k}$-integrated spectra (see Fig. 7h-j). First, the site- and orbital projected spectral function $A_{\mathrm{proj}}(\omega)$, defined by projecting the Bloch-resolved spectral function $A_\nu(\mathbf{k}, \omega)$ with Bloch index ν onto a chosen site-orbital and summing over $\mathbf{k}$. Note that this function is comparable but strictly not identical to the local spectral function A_{loc}, which is obtained from analytical continuation of the local Green's function. Second, it proves instructive to also plot directly $A_\nu(\omega)$, i.e. the $\mathbf{k}$-integrated Bloch-resolved spectrum.

This allows us to trace the behavior of the former DFT bands upon interaction and displays the QP formation originating in Bloch space.

The projected spectrum of $PdCoO_2$ exhibits the near subshell filling of Co($3d$) and the Pd dominance of the low-energy QP peak at the Fermi level. While on a first glance, $A_{\rm proj}$ for the Cr($3d$) spectrum in $PdCrO_2$ looks similar to the previous Co($3d$) one, the physics is completely different; the Cr-t_{2g} states are in a Mott state and therefore their spectral weight is shifted to deeper energies up and below the Fermi level, i.e. to upper and lower Hubbard bands. The Cr-e_g states are mostly empty, but show also strong incoherence effects in Fig. 7b. Mott criticality in the CrO_2 layers has been originally suggested by several experiments from strong hints for localized Cr^{3+} $S = 3/2$ spins [9, 65, 67]. The QP peak at low energy is of dominant Pd($4d$) character, therefore confirming the previously announced mechanism of a correlation-induced shift of a DFT-original deeper lying Pd-dominated band towards $\varepsilon_{\rm F}$. The projected $AgCrO_2$ spectrum shows again the Mott-insulating Cr($3d$) part along with the band-insulating Ag($4d$) part. The plots of $A_\nu(\omega)$ render obvious that for $PdCoO_2$ the low-energy QP is for the most part constituted from a single Pd-dominated Bloch dispersion, which we call *LE-Pd*. The same holds for the $PdCrO_2$ case. Yet importantly, both QP peaks display the hybridizing contribution of Co/Cr-dominated functions, and the LE-Pd function moreover exhibts significant energy dependence. Both features point to the relevance of the subtle impact of electronic correlation onto the low-energy regime. Or in other words, the 'single-band' dispersion crossing $\varepsilon_{\rm F}$, though not dominated by the strongly-interacting $\mathcal{B}$-site $3d$ orbitals, still carries subtle effects of correlations which most certainly rule (parts of) the challenging delafossite physics. But be aware of our difference in nomenclature; 'cPd' denotes the complete single low-energy dispersion, while 'LE-Pd' marks the most dominant A_ν contribution to it. The corresponding A_ν plot for $AgCrO_2$ shows that the band-insulating character part is equally dominated by a single LE-Ag dispersion, with the Mott-insulating character part once again carried by Cr($3d$).

Finally note that the O($2p$) states are mostly aligned with Ag($4d$) in $AgCrO_2$, whereas they are located significantly deeper in energy than Pd($4d$) in $PdCoO_2$ and $PdCrO_2$.

3.3.2 Key correlation features and concepts

After this overview, we want in the following discuss and comment on relevant underlying electron correlation aspects. First, the atomic-like picture of a fully-closed Co-t_{2g} subshell in the $PdCoO_2$ compound is of course an idealization. The DFT+DMFT occupancies per single orbital on Co at room temperature amount to $\{n_{e'_g}, n_{a_{1g}}\} = \{1.90, 1.93\}$, thus there is still about 4% local t_{2g} doping. The associated charge fluctuations together with the hybridizations on the low-energy QP dispersion point to a subtle connection between the Pd layer and the CoO_2 layer. This is underlined by the spectral comparison shown in Fig. 8, where one may observe that the $\varepsilon_{\rm F}$-slope of the cPd dispersion, i.e. the Fermi velocity, has slightly *increased* with correlations. Usually, strong local electronic correlations lead to a reduction of the QP Fermi velocity, associated with a bandwidth renormalization toward smaller values. Yet here, the explicit Coulomb interactions are active in the CoO_2 layer and the cPd dispersion with dominant Pd($4d$) weight mainly originates from the 'non-interacting' Pd layer. Seemingly, an

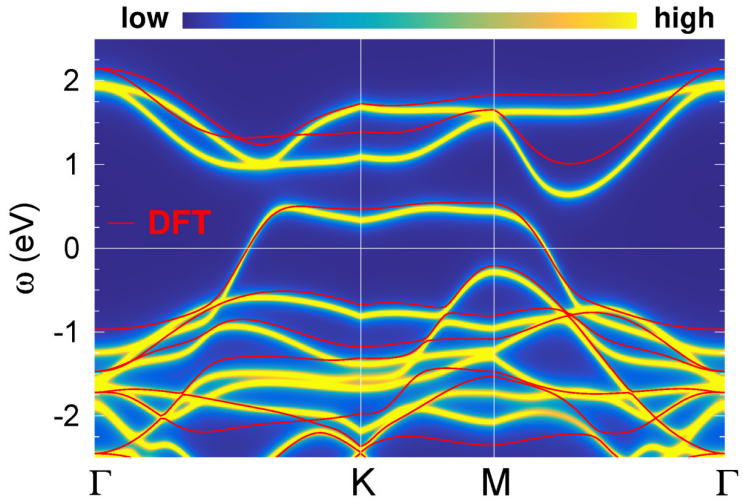

Figure 8: Comparison of the DFT band structure (red) and the DFT+DMFT spectral function of $PdCoO_2$.

implicit nonlocal effect of correlation steepens the dispersion, at least on a proof-of-principle level. This could be a contributing factor to the high conductivity of $PdCoO_2$. Again, (local) correlation effects appear not decisive in $PdCoO_2$, but their role still deserves further exploration.

The impact of electronic correlations is obviously crucial for $PdCrO_2$. On a more formal level, interactions lead to a unique metal-to-metal transition between a system with Cr($3d$)-dominated threefold dispersion at weak coupling and a system with Pd($4d$)-dominated single dispersion at strong coupling. The question arises how this apparent quantum phase transition takes place with increasing interaction strength U. Figure 9 displays the spectral function and fatbands for the DFT limit ('$U = 0$') and for $U = 1.5\,\mathrm{eV}$, i.e. half the assumed correct interaction strength in $PdCrO_2$, in direct comparison. Of course, the $U = 0$ data is identical to what is shown in Fig. 5, rendering the mechanism for the transition clear: The three bands at the Fermi level are filled with two electrons, and hence four electrons populate the altogether four bands when counting down in energy from ε_F. These four bands are of mixed Cr($3d$), Pd($4d$) character, with dominance from the $3d$ sector. Due to the given band entanglement, strong correlations transform three of them into Hubbard bands, and leave a resulting one with half filling at the Fermi level. Interestingly, for the intermediate coupling in Fig. 9b, the system adopts a 'strange' situation. The Cr-t_{2g} dispersion are very incoherent and not yet Mott localized, and the cPd dispersion is not yet fully established coherently. Note that especially the cPd dispersion, which appears weakly-interacting at strong and weak coupling, is intriguingly affected by correlations close to the given metal-to-metal transition. This underlines the intricate inter-layer physics that is at work in $PdCrO_2$ with its 'hidden-Mott' state. Note that in a pure model context, at least three bands would be necessary to capture a hidden-Mott scenario: one fully filled band and two bands with overall quarter filling when putting interactions to zero. Strong interactions should then transfer one electron from the filled band to both remaining bands, rendering them

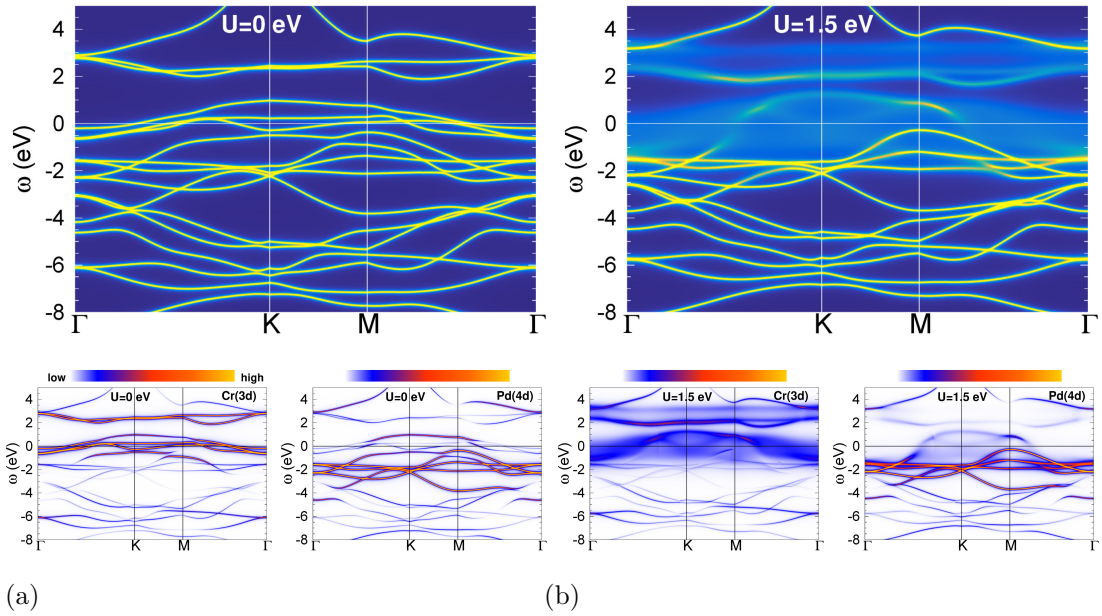

Figure 9: Spectral properties of $PdCrO_2$ for different interaction strengths: (a) $U = 0\,\mathrm{eV}$, i.e. DFT bands, and (b) $U = 1.5\,\mathrm{eV}$. Top: spectral function, bottom: fatbands for Cr($3d$) (left) and Pd($4d$) (right) (from [66]).

half filled.

From a model perspective of correlated electrons, Kondo-lattice type of Hamiltonians describing strongly-interacting sites within a Fermi sea [68, 69] have been discussed as a starting perspective for $PdCrO_2$ [10]. Such a framework has then indeed put into practise in order to account for the coupling of the Cr spins to the Pd layer in the magnetically-ordered state [11]. However, as already mentioned in Ref. [10], a standard Kondo-lattice model of spins coupled to free electrons appears too simplistic to cover the full complexity of the above described hidden-Mott physics. Modelling the electronic correlations that originate from the CrO_2 layer and spanning over to the Pd layer in a comprehensive way has most definitely to account for the outlined metal-to-metal transition.

Because of the $4d^{10}$ state of silver in $AgCrO_2$, an intricate band entanglement as in $PdCrO_2$ is missing. In the DFT limit, the three Cr-t_{2g} bands at the Fermi level are already half filled with three electrons. Thus the internal Mott transition in the CrO_2 layers does not lead to a metal-to-metal transition, but to a more ordinary metal-to-insulator transition with increasing U. But there is a twist; the valence-band maximum of insulating $AgCrO_2$ is dominated by silver (and oxygen) character, highlighting the band-insulating aspect of the system. The compound is therefore best coined as *band-Mott insulator*.

To emphasize the key differences of the given delafossites from a minimal perspective, Fig. 10 summarizes the main features from the noted four-band perspective of $\mathcal{B}$-site derived t_{2g} bands and $\mathcal{A}$-site derived uppermost $4d$ band part.

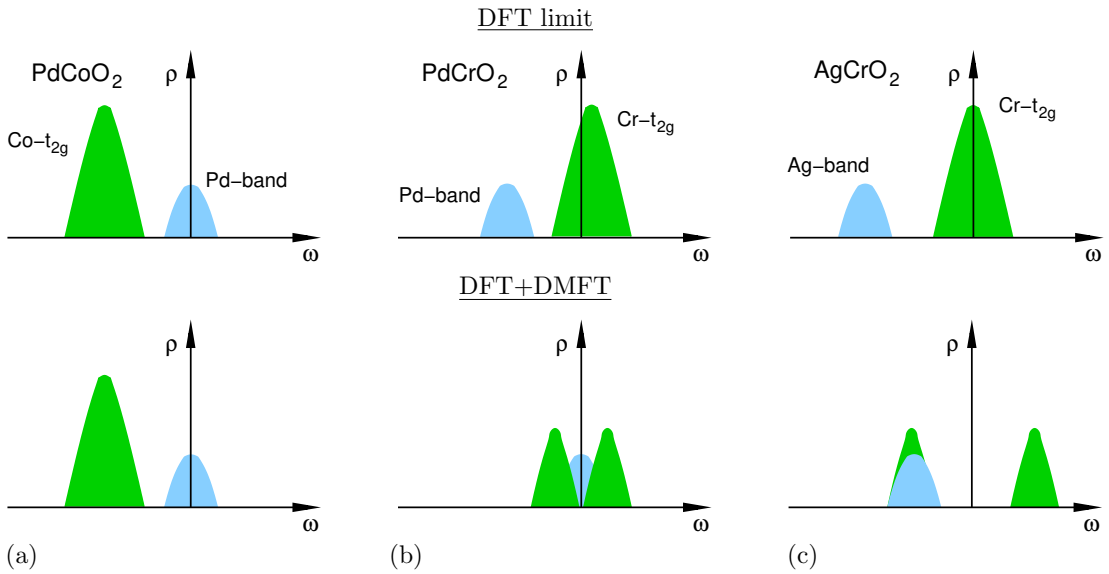

Figure 10: Sketch of the basic differences in the **k**-integrated spectral function $\rho(\omega)$ for the most-relevant four bands close to the Fermi level among the studied delafossites. Top: DFT limit, bottom: DFT+DMFT. (a) $PdCoO_2$: Co-t_{2g} bands occupied, uppermost Pd($4d$)-band half filled. (b) hidden-Mott $PdCrO_2$: Cr-t_{2g} bands 1/3 filled, uppermost Pd($4d$)-band occupied. (b) band-Mott insulating $AgCrO_2$: Cr-t_{2g} bands half filled, uppermost Ag($4d$)-band occupied.

4 Mott design of correlated delafossites

4.1 General considerations

We have seen in the last section that in an interacting many-body sense, the revealed correlation effects in $PdCoO_2$ and $AgCrO_2$ are apparently not yet of particular breathtaking kind. The former compound is a straightforward metal with, from the current viewpoint, weak impact of correlations. The latter compound harbors strong correlations and is a combined band-Mott insulator, yet a Mott-insulating state per se is not a spectacular state of matter. On the other hand, the $PdCrO_2$ compound seems quite exotic with its entanglement between metallic and Mott-insulating characteristics. However in the equilibrium state, $PdCrO_2$ behaves like an ordinary metal, even across the Néel temperature and in the ordered AFM phase [67]. The hidden-Mott state in the system is seemingly behaving like a 'sleeping dragon'. For its awakening and the display of more exciting physics, one has to drive the compound 'out of its comfort zone' by disturbance and further design.

Hence in the following subsections the focus will be on possible theoretical ways how to 'wake up the dragon' and to create new correlation phenomenology out of the intriguing scenario found in $PdCrO_2$. We will here only briefly comment on point-defect and pressure/strain effects in subsection 4.2, and will discuss in some more detail the effects of heterostructuring in subsection 4.3. An overview on recent experimental activities towards engineering correlated delafossites will close this section.

4.2 Defect engineering, pressure and strain

Chemical doping either iso-valent or of charge-doping kind is a traditional route to modify a given electronic structure. The hole- and electron doping of cuprates by substitutional impurities which transfers a stoichiometric Mott insulator into a high-T_c superconductor represents the most famous example [70]. Melting the instrinsic Mott insulator in $PdCrO_2$ by defect-induced charge doping becomes indeed possible from supercell DFT+DMFT calculations in a corresponding dense-defect regime with symmetry breakings due to local point defects. On the other hand, small charge doping on the Cr site performed in a virtual-crystal approximation leads to a transfer of doping charge from the CrO_2 layers to the Pd layers, thus doping mainly the metallic band. We refer the reader to Ref. [10] for further details.

Additionally, iso-valent chemical doping may be promising from the metal-to-metal transition viewpoint given above. Namely, introducing e.g. Mo impurities on the Cr sublattice should lead to a reduction of the effective U in the d-shell on the $\mathcal{B}$ site, enabling access to the intriguing intermediate-coupling regime.

Application of pressure or strain can also result in a relevant change of the electronic structure. For instance, uniaxial pressure/strain along the c-axis would modify the Pd and CrO_2 layer separation, which may effect the band entanglement and the hidden-Mott physics.

4.3 $PdCrO_2$-$AgCrO_2$ heterostructures

As noted in the introduction and became clearer in section 3, delafossites may be viewed as natural heterostructures with different electronic characteristics in the $\mathcal{A}$- and $\mathcal{B}O_2$-layers. It may be therefore obvious that a merging of delafossite physics and the ever-growing field of oxide heterostructures (see e.g. Refs. [71, 72] for reviews) could turn out as a frutiful combination.

In fact, heterostructures from combining $PdCrO_2$ and $AgCrO_2$ may be of particular interest. Both compounds have similar lattice parameters, resulting in a minor mismatch, and differ only by one electron in the $\mathcal{A}$-site valence. However their electronic phenomenology, i.e. hidden-Mott metal vs. band-Mott insulator, is quite different. Heterostructuring both delafossites provides therefore a unique doping scenario: by keeping the local environment rather undisturbed, filling modifications in the Cr-t_{2g} manifold (i.e. green spectra in Figs. 10b,c) inbetween the DFT-limit values may be triggered. In the following we denote the DFT filling fraction of the Cr-t_{2g} states by α. Than the given heterostructures formally interpolate directly between the hidden-Mott metal ($\alpha = 1/3$) and the band-Mott insulator ($\alpha = 1/2$), and should show via which path both phases are connected.

Alternate stackings of Pd, CrO_2 and Ag layers, i.e. straightforward *out-of-plane* heterostructures, are a natural realization of such a scenario, and is discussed in section 4.3.1. Note that a 'simple' interface construction between wide blocks of $PdCrO_2$ and $AgCrO_2$ might not be an ideal research object, since presumably, most of the interface modifications to transport would be masked by the metallic $PdCrO_2$ block. However, another type of heterostructure may also be promising, namely an *in-plane* variation within the $\mathcal{A}$ layer from intermixing the Pd and Ag content in an ordered fashion. This type should not be immediately linked to the doping scenario described above, because of the inherent change of the $\mathcal{A}$-layer character. But it could benefit

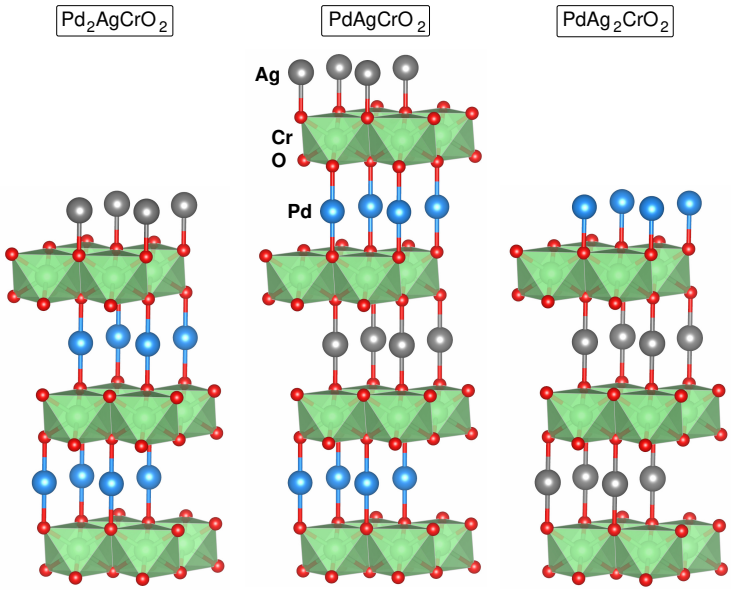

Figure 11: Crystal structures of the designed out-of-plane heterostructures with stacking along the c-axis. Pd_2AgCrO_2, $PdAgCrO_2$ and $PdAg_2CrO_2$ (from left to right). Pd: blue, Ag: grey, Cr: green and O: red. From Ref. [66].

from the specific delafossite layer (dis)entangling, and as described in section 4.3.2, possibly give rise to the different unique scenario of a designed 2D lattice within a Mott background.

4.3.1 Out-of-plane heterostructures: correlated semimetallic states

Three heterostructures with different $PdCrO_2/AgCrO_2$ stacking along the c-axis are designed, namely Pd_2AgCrO_2, $PdAgCrO_2$ and $PdAg_2CrO_2$ (see Fig. 11). The lattice parameters are chosen from linear-interpolating the respective experimental data of the bulk structures (cf. Tab. 1), and the Hubbard U (identical on every Cr site) is also correspondingly interpolated from the limiting delafossite cases (see Ref. [66] for further details).

Before discussing the numerical results, let us briefly brainstorm about the electronic structure condition. From the $PdCrO_2$ perspective, the additional blocking layers of Ag kind as well as the stronger Mott-insulating character induced therefrom into the CrO_2 layers should increase correlations within the Pd layers, too. But this will again happen in a more subtle way than in standard correlated systems, where an associated Coulomb repulsion for such a layer is increased when looking for stronger correlation effects. Remember that there is no Hubbard U on Pd and all correlation increase has to take place in a nonlocal way from the surrounding layers. Thus, the present heterostructures pose a quite original correlation problem at low energy; a half-filled Pd layer without intra-layer interaction, subject to rising 'Coulomb pressure and confinement' imposed from the neigboring layers. How does the single electron of dominant Pd($4d$) character cope with that situation?

Figure 12 displays the summarized DFT+DMFT spectral properties at room temperature for the three heterostructures. A detailed discussion, also concenrning stability issues and with

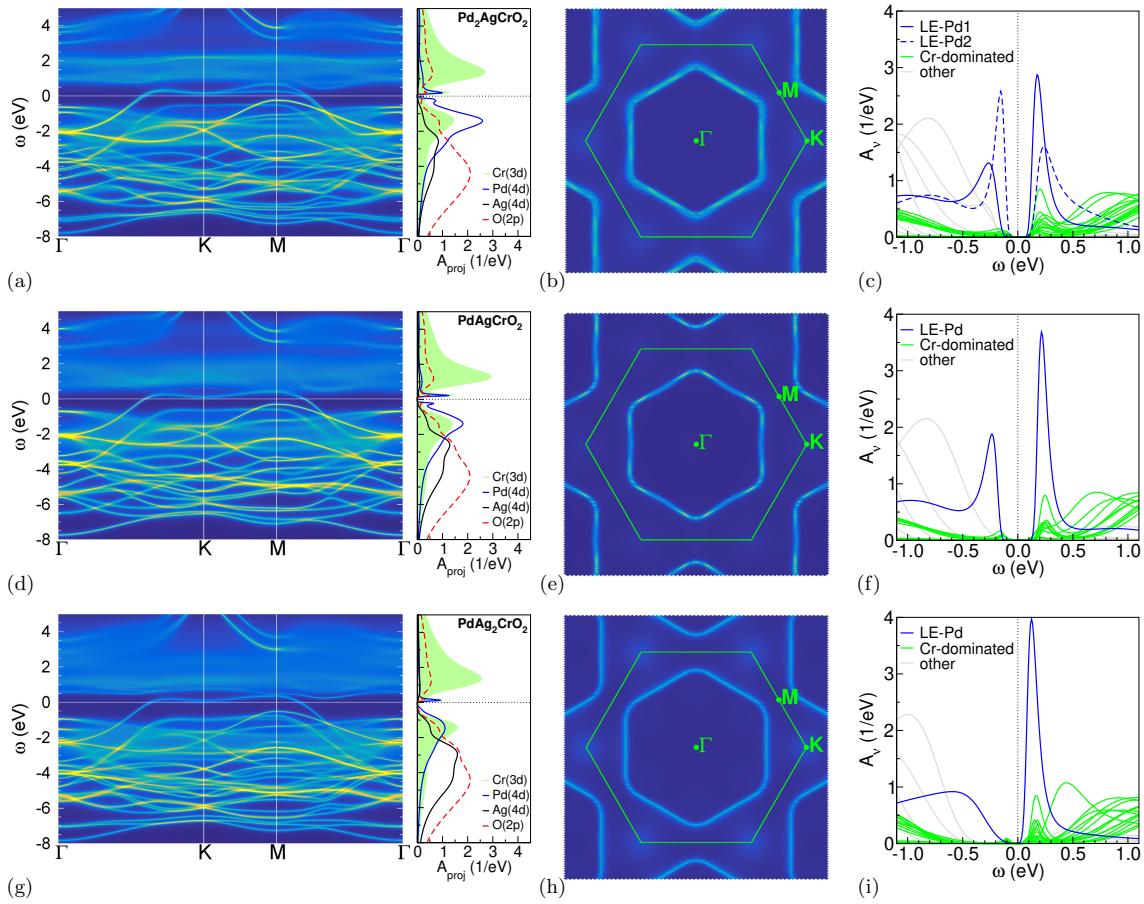

Figure 12: Paramagnetic DFT+DMFT spectral data for the designed heterostructures: (a-c) Pd_2AgCrO_2, (d-f) $PdAgCrO_2$ and (g-i) $PdAg_2CrO_2$. (a,d,g) Spectral function $A(\mathbf{k},\omega)$ along high-symmetry lines in the $k_z = 0$ plane of reciprocal space (left) and $\mathbf{k}$-integrated site- and orbital-projected spectral function (right). (b,e,h) Fermi surface for $k_z = 0$ within the first Brillouin zone (green hexagon). (c,f,i) $\mathbf{k}$-integrated Bloch contribution $A_\nu(\omega)$ with characterization of dominance. From Ref. [66].

extension to lower-temperature properties, can be found in Ref. [66]. The main result, common to all structural cases, may be extracted from the low-energy comparison of the $\mathbf{k}$-resolved and the $\mathbf{k}$-integrated data: while there are still QP-like dispersions visible in $A(\mathbf{k},\omega)$ at the Fermi level, the integrated spectra shows vanishing spectral weight at ε_F. We coin this puzzling electronic state as *correlation-induced semimetal (CIS)*, which is obviously a result of the intriguing correlation scenario described above. Upon rising obstruction of transport, the key Pd($4d$) electron can neither localize in real space (as in a Mott insulator) nor rest in a filled band (as in a band insulator). Hence it reduces the low-energy spectral weight as much as possible for an intact half-filled band, resulting in the CIS state. In some sense it amounts to a very strong reduction of the usual QP coherence scale of strongly correlated electrons, yet by still keeping the 'coherence' of the original dispersion. To our knowledge, such a rather exotic electronic state has not yet been reported in correlated matter and it awaits experimental verification.

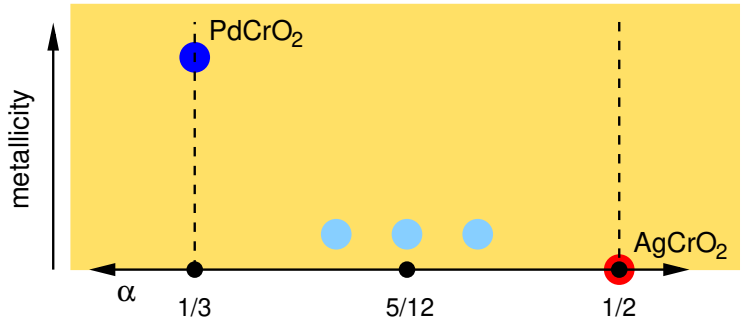

Figure 13: Room-temperature metallicity of the $PdCrO_2/AgCrO_2$ out-of-plane heterostructures with respect to the DFT filling factor α of the Cr-t_{2g} bands. Blue: metal $PdCrO_2$, red: band-Mott insulator $AgCrO_2$, and lightblue: CIS Pd_2AgCrO_2, $PdAgCrO_2$, $PdAg_2CrO_2$ (from left to right).

Since the effective $\mathcal{A}$-site occupation is modified from the alternate-stacking architecture, the problem can also be pictured from an alternative viewpoint, namely from a formal change of the DFT filling factor α of Cr-t_{2g} (cf. Fig. 10). The α values for the given heterostructures may formally be assigned by linear interpolation of the values for $PdCrO_2$ ($\alpha = 1/3$) and $AgCrO_2$ ($\alpha = 1/2$). Accordingly, the metallicity with respect to α is depicted in Fig. 13. The transformation of the CIS states to the hidden-Mott state or the band-Mott insulator of the respective bulk compounds may be studied with different heterostructure layerings. It is very likely from Fig. 7i and Fig. 12i, that inbetween the CIS and the band-Mott insulator, there is another metallic regime. Notably, hole doping of the band-Mott-insulating state implements charge carrier into the more dominant band-insulating part of $AgCrO_2$. A doping $\alpha > 1/2$ cannot be facilitated anymore by changing the $\mathcal{A}$-site TM($4d$) ion, but modifying the $\mathcal{B}$-site TM($3d$) might work. The regime $\alpha < 1/3$ could in principle be reached by replacing Pd with Rh. But the Rh^+ ion with $4d^8$ configuration appears non-existing in known solid-state materials, and henceforth the stability of $RhCrO_2$ delafossite is very unlikely.

Still in a Gedankenexperiment, since also instructive for the understanding of the hidden-Mott state, we performed calculations for hypothetical $RhCrO_2$, using the lattice parameters and Hubbard U of $PdCrO_2$. The results are shown in Fig. 14. The DFT band structure at lower energy exhibits the expected upward shiftings of the dispersions compared to the Pd compound. The filling of the Cr-t_{2g} dominated bands is hence smaller, close to unity (i.e. $\alpha \sim 1/6$). Surprisingly, interactions still establish a near hidden-Mott state with a half-filled Cr-t_{2g} subshell. This underlines the significant coupling between the $\mathcal{A}$ layer and the CrO_2 planes. The fermiology becomes twofold in the Rh compound, associated with a shrinking of the original warped hexagonal sheet and the appearance of novel hole sheets around M (periodically arranged in a sixfold way). Note that Γ- and M-sheet nearly touch in a Dirac-like crossing along Γ-M. The appearance of the M-sheet is not that surprising, since the corresponding dispersion with the maximum at M is observed just below the Fermi level in $PdCrO_2$ (cf. Fig. 7b). Finally, the two-band picture is completed by observing two dominant LE-Rh contributions $A_\nu(\omega)$ close to

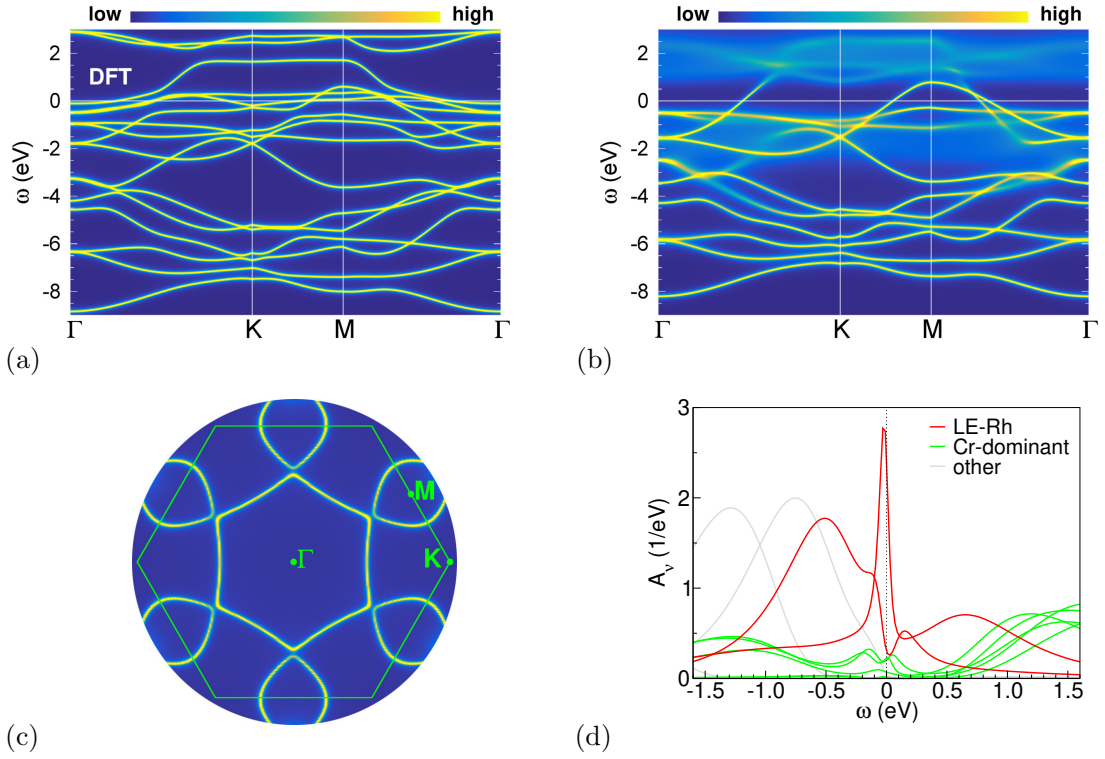

Figure 14: Spectral properties of hypothetical $RhCrO_2$. (a) DFT band structure, (b-d) DFT+DMFT features: (b) spectral function $A(\mathbf{k}, \omega)$, (c) Fermi surface and (d) $\mathbf{k}$-integrated Bloch contribution $A_\nu(\omega)$ with characterization of dominance.

ε_F. Furthermore, Fig. 14d displays that the Cr-t_{2g} dominated dispersions are not completely transformed into Hubbard bands by interactions, but show reduced weight at the Fermi level. In conclusion, if existing, $RhCrO_2$ would be a two-band metal with even stronger entangling between Cr($3d$) and TM($4d$). Reaching such a two-band regime in metallic delafossite, possibly by different doping/engineering routes of $PdCrO_2$, would be highly interesting.

4.3.2 In-plane alternations: Dirac(-like) states and emergent flat-band physics

Let us now push the limits of conceivable delafossite engineering even somewhat further, by interpreting the metallic implication of Pd in $PdCrO_2$ and the band-insulating implication of Ag in $AgCrO_2$ theoretically footlose. Instead of engineering $PdCrO_2$ 'out of plane' from replacing Pd layers by Ag layers, one may imagine an 'in-plane' alternation from replacing Pd sites by Ag sites in the periodically-repeated $\mathcal{A}$ layer. As a result, a novel natural-heterostructure delafossite emerges, but now with a decorated $\mathcal{A}$ layer. The viewpoint behind arises from picturing the $\mathcal{A}$ layer in hidden-Mott delafossite as a canonical single-band triangular lattice at half filling, embedded in a Mott-insulating background. By manipulating the features of this triangular lattice, a unique platform for studying correlation effects in such a Mott background may be generated. The simplest manipulations in this regard are given by the straightforward transformations of the original triangular lattice via the K- and M-point ordering instabilities,

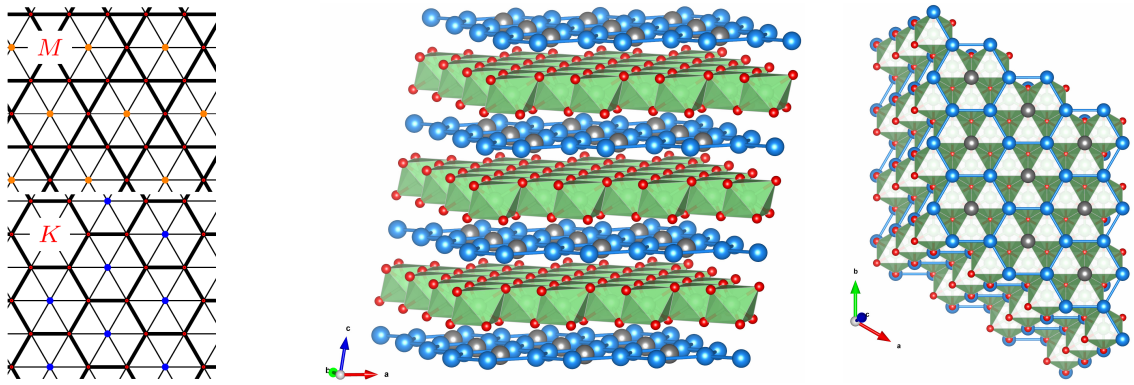

Figure 15: In-plane design of the $\mathcal{A}$ layer in delafossites. (a) Natural triangular-lattice ordering instabilities of K-point (honeycomb) and M-point (kagomé) kind (from [78]). (b) Effective honeycomb delafossite, from understanding Pd(Ag) positions as active(blocking) sites; Pd: blue, Ag: grey, O: red; Cr: green. Left: 3D view and right: view onto the effective honeycomb lattice of Pd sites.

associated with the honeycomb (K) and the kagomé (M) lattice (see Fig. 15a). Realizing those lattices within a Mott background is exciting because they host Dirac-semimetallic and in the case of the kagomé lattice additionally flat-band dispersions. The study of these unique dispersion features under the possible influence of strong correlations is a recent emerging research field in condensed matter, see e.g. Refs. [73–75].

To facilitate this reductions of the triangular lattice, the introduction of periodic blocking sites which ideally disconnect hopping processes, can be a promising route. This concept has been e.g. used to account for the effect of charge ordering onto transport properties in Na_xCoO_2 [76, 77]. From the nominal Ag($4d$) filled-shell in the CrO_2-based delafossites, we *assume* in the present context that Ag sites within the Pd layer may serve as such blocking sites. For sure, finite covalency will only realize a partial blocking, however, this may still be sufficient to mimic basic honeycomb- or kagomé-lattice features. To realize a honeycomb(kagomé) lattice in that spirit within the $\mathcal{A}$ layer, one out of three(four) in-plane Pd sites has to be replaced by Ag. Note that though preparing such orderings in the lab will be surely demanding, a layer-by-layer growth might still be feasible from tailoring the layer stoichiometry. If the given Pd-Ag in-plane orderings are thermodynamically stable (for given temperature, pressure, strain, etc.), nature will take its course in realizing the periodic effective honeycomb/kagomé pattern. For the honeycomb case, Figs. 15b,c depicts the designed delafossite structure. The DFT+DMFT calculations for both effective-lattice systems are again performed with corresponding linear interpolation of the known lattice parameters and the chosen Hubbard U values for the bulk compounds. The honeycomb(kagomé) structure asks for a supercell of three(four) original formula units.

In Fig. 16 we first show the spectral function of the effective honeycomb structure. From graphene studies it is well known that the nearest-neighbor (NN) tight-binding electronic structure of the half-filled honeycomb lattice is semimetallic, with prominent Dirac dispersions (i.e.

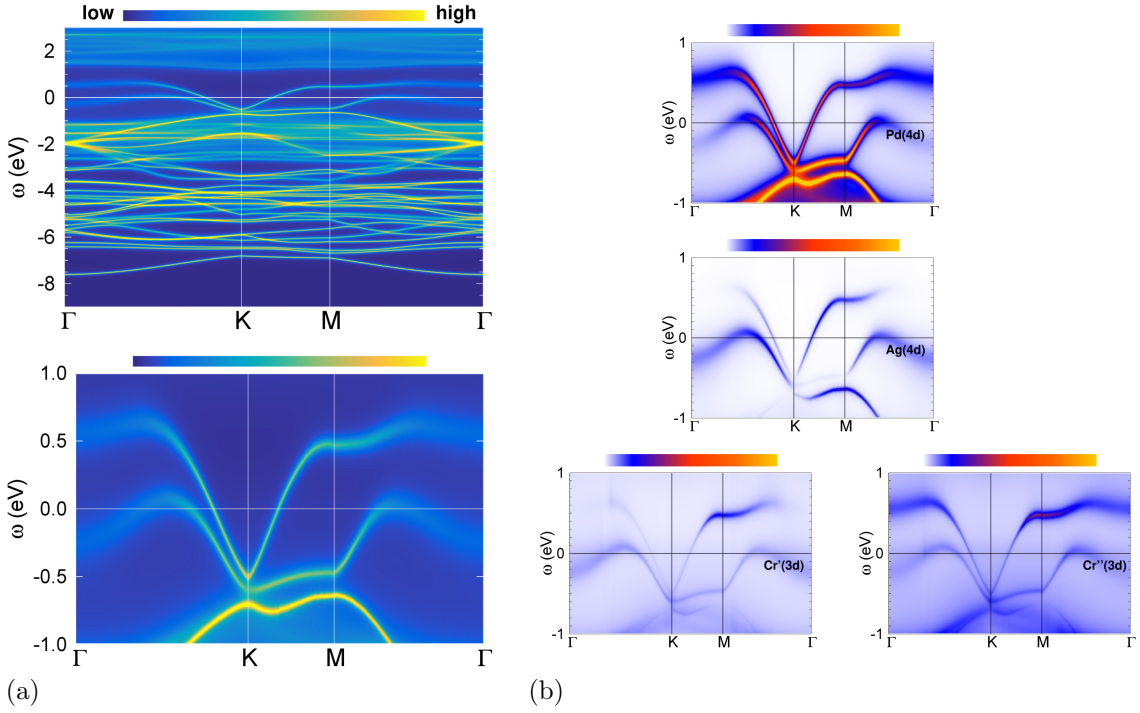

Figure 16: Interacting spectrum of effective-honeycomb (Pd,Ag)CrO_2 from DFT+DMFT at $T = 193\,\mathrm{K}$. (a) Spectral function in (top) larger and (bottom) smaller energy window. (b) Orbital-site content ('fatbands'), from top to bottom: Pd($4d$), Ag($4d$) as well as both symmetry-inequivalent Cr($3d$), i.e. Cr'($3d$) and Cr"($3d$).

massless Dirac fermions) at the K point in reciprocal space [79]. The low-energy spectrum of the present effective lattice in the delafossite setting shows indeed some resemblance of this feature. First, the CrO_2 planes remain Mott-insulating upon the in-plane (Pd,Ag) structuring and there are two Pd-dominated dispersion close to ε_F (see Fig. 16a). A Dirac-like dispersion around K is indicated, yet shifted, with different filling and different overall dispersion compared to graphene. Still, some blocking behavior of Ag is realized, transforming the original $PdCrO_2$ low-energy dispersion in direction towards the canonical honeycomb dispersion. The site-orbital content in Fig. 16b renders obvious that Ag($4d$) and Cr($3d$) have quite a weight on the twofold dispersion around the Fermi level, highlighting the entangled nature. Note that there are two symmetry-inequivalent Cr positions, with Cr' mirroring the position of the blocking site within the Cr sublattice.

The NN tight-binding electronic structure of the kagomé lattice is known for its flat-band feature at one side of the band edge, as well as for the Dirac dispersion at 4/3(2/3) filling depending of the sign of the NN hopping (e.g. [73]). In the present case, the flat-band feature should appear at the upper band edge and thus the Dirac point at 2/3 filling. Figure 17 depicts the resulting spectral function of effective-kagomé (Pd,Ag)CrO_2, and from a brief look the canonical kagomé features are hard to decypher. The intriguing effect of correlations and only-partial Ag blocking render things hard to read. Yet after a closer look, and after also comparing

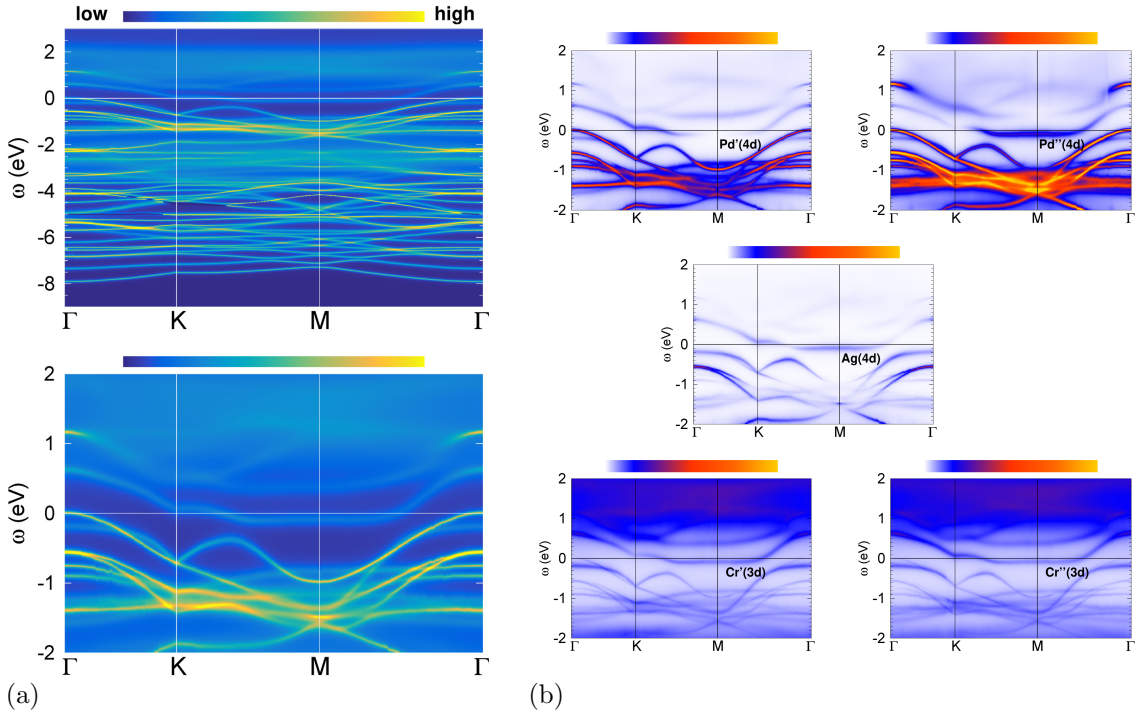

Figure 17: Interacting spectrum of effective-kagomé (Pd,Ag)CrO_2 from DFT+DMFT at $T = 193\,\mathrm{K}$. (a) Spectral function in (top) larger and (bottom) smaller energy window. (b) Orbital-site content ('fatbands'), from top to bottom: both symmetry-inequivalent Pd($4d$), i.e. Pd'($4d$) and Pd"($4d$), Ag($4d$) as well as both symmetry-inequivalent Cr($3d$), i.e. Cr'($3d$) and Cr"($3d$).

with the non-interacting DFT states, the remains of the flat-band feature can be located around 1 eV above the Fermi level. Interestingly, the interactions in the delafossite structure seemingly transfer spectral weight from there towards ε_F. Close to Γ, a waterfall-like spectral signature may be observed. Hence a flat, but at $T = 193\,\mathrm{K}$ rather incoherent, low-energy feature ranging from K to M and halfways to Γ emerges (see Fig. 17a). Its spectral content is dominated by the symmetry-equivalent subclass Pd"($4d$), which collects two out of the three in-plane Pd sites of the supercell. But again, contribution from once more formally Mott-insulating Cr($3d$) is not negligible. The Dirac-dispersion feature at K from the canonical kagomé lattice can also be identified at about -0.6 eV. Thus tough again the finite covalency of in-plane Ag does not allow for complete blockings, and also the original half-filled nature of the Pd layer in $PdCrO_2$ is disturbed by introducing Ag, the interplay of the hidden-Mott physics with model-kagomé features gives rise to interesting low-energy behavior.

In conclusion, expectedly neither the effective-honeycomb nor the effective-kagomé lattice realization in the modifed $PdCrO_2$ structure enables canonical textbook dispersions at the Fermi level. But as a proof of principles, the in-plane engineering of delafossites may be a route to create nontrivial low-energy dispersions which are subject to the puzzling layer-entangled correlation delafossite physics.

4.4 Experimental work on engineering correlated delafossites

After discussing some theoretical designing ideas, let us finally have a quick look on the current status of designing and manipulating correlated delafossites in experiment.

The preparation of bulk single crystals has been demanding for quite some years, but nowadays does not really pose a tough problem anymore for the known delafossites. They are nowadays even used as electrocatalyst for hydrogen evolution reactions [80]. However, layer-by-layer growth from e.g. pulsed-laser deposition (PLD) or molecular-beam epitaxy (MBE), especially for the metallic systems, remained challenging until recently. But starting from about two years ago, the number of successful reports on grown metallic delafossites is increasing. For instance, thin-film preparation of $PdCoO_2$ [81–84] and $PdCrO_2$ [85, 86] has been reported by several groups. The transport properties of such films share in most cases the exceptional high conductivity known from the bulk compounds, and device-oriented ideas have been proposed [87]. Notably, in the ultra-thin limit of $PdCrO_2$ films grown on a single-layer of $CuCrO_2$, a significant increase of resistivity is reported [85].

Recent surface-sensitive studies on metallic delafossites are furthermore promising in revealing details on the impact of correlations. Strong Rashba-like spin splitting in CoO_2 and RhO_2 related delafossite surface states [88] and itinerant ferromagnetism on the Pd-terminated (polar) surface of $PdCoO_2$ [89, 90] have been observed.

Chemical doping and/or introduction of reasonable amounts of point defects through irradiation appears quite difficult in metallic delafossites [91]. Systematic studies on substitutional doping are very rare [92]. Apparently, the high-purity crystal state of these materials [8] renders it on the other hand hard to implant a sizable amounts of point defects.

Nonetheless, the research activity on (metallic/correlated) delafossites is high and expected to further increase. Experimental investigations on specifically designed delafossites, e.g. along the lines of the theoretical propositions discussed in section 4.3, are believed to become available soon.

5 Conclusions and outlook

Delafossites are not new materials in condensed matter physics. They have been around for quite some time and also strong correlation phenomena have been discussed e.g. in the context of insulating Cu-based compounds within the early days of high-T_c cuprate research. Yet the concise studies of high-purity metallic delafossites that started about ten years ago brought them (back) into the spotlight of condensed matter research. Though known as the best-conducting oxides, they still share the inherent property of hosting strongly correlated electrons common to most transition-metal oxides. But whereas in standard Mott materials such as e.g. V_2O_3, $YTiO_3$ or La_2CuO_4 the competition between Coulomb repulsion and itinerancy establishes an overall Mott-insulating state (or a metal-insulator transition with temperature), electron correlations in delafossites act much more subtle and their characteristics can be quite elusive. In the extreme limit of CrO_2-based delafossites, they can give rise to layer-selective Mottness which is then coupled to the remaining metallic and/or band-insulating layers in an unusual way.

What makes delafossites so different from other oxides? The dumbbell-bond separation between the $\mathcal{A}$ and $\mathcal{B}O_2$ layers leaves them rather "freestanding", which enables a seemingly independent electronic behavior. As a result, the scattering within the $\mathcal{A}$ layer and from there with the $\mathcal{B}O_2$ layers is surprisingly small, for reasons which very details still need further exploration. Notwithstanding, a delicate coupling between both layer types prevails, as e.g. displayed by the here presented results of the correlation-induced increase of Fermi velocity in $PdCoO_2$ and the metal-to-metal transition with increasing U in hidden-Mott $PdCrO_2$. In the general correlation context, the latter compound stands out and is undoubtly the most 'enigmatic' delafossite. But in standard measurements of transport and spectroscopic behavior, there are (yet) no dramatic signs of its unusual correlated nature. The recent photoemission study of Sunko *et al.* [11], which speculates about spin-charge separation in $PdCrO_2$, appears as an important experimental step to face its correlated phenomenology. Albeit driving the system out of its 'comfort zone' seems necessary to unravel more facets of correlated electrons in $PdCrO_2$.

There is a broad literature on the magnetism of $PdCrO_2$ and related spin-active delafossites, e.g. Refs. [11, 93–100], but in this short review we focussed on the paramagnetic correlation aspects. The magnetic properties are surely a relevant feature and based on correlations. However as often the case in TM oxides, those properties seem secondary once strong correlations have been established. For instance, the 120° ordering at lower temperature in $PdCrO_2$ and $AgCrO_2$ may only set in after the Mott-critical behavior with strong local $S = 3/2$ spin formation in the CrO_2 layers is realized. A deeper understanding of the underlying exchange mechanisms should therefore ask for a thorough account of the correlated-electron states. Still, the spin degree of freedom might be key to access the delafossite many-body physics by experimental means.

As we stressed several times, the design aspect comes in naturally when engaging oneself with delafossites. The bulk compounds are comparably simple in structure and there are various different delafossites ranging from metallic to insulating. Plus, they may host such intriguing phases as the hidden-Mott phase. Hence taking advantage of this potentially plethora of design possibilities is tempting and we tried to discuss some ideas in that direction in the present text. Besides magnetism, we also left out the aspect of topology. The latter is very prominent in modern condensed matter research, and could also play a vital role in engineered delafossites. One may surely imagine architectures hosting nontrivial topological fermions within the unique layer-selective Mott background of strongly correlated delafossites. A first minimal step towards such scenarios has been indicated by unveiling Dirac(-like) dispersions by design in section 4.3.2.

To conclude, albeit delafossites have not yet entered the biggest stage of condensed matter physics, they surely are a 'colorful' addition to the realm of correlated materials. It is hoped that this brief review stimulates further theoretical and experimental research in finding ways to unleash the so far mostly hidden nature of strong electronic correlations in delafossites.

Acknowledgments

The author is indebted to H. O. Jeschke, P. D. C. King, I. Krivenko, A. P. Mackenzie, L. Pourovskii, R. Richter, A. W. Rost, V. Sunko and P. Wahl for helpful discussions on various facets of delafossites as well as on computational aspects. Financial support from the DFG LE-

2446/4-1 project “Design of strongly correlated materials” is acknowledged. Computations were performed at the JUWELS Cluster of the Jülich Supercomputing Centre (JSC) under project number hhh08.

References

[1] Friedel C 1873 *Compt. Rend. Acad. Sei. Paris* **77** 211

[2] Rogers A F 1913 *Amer. Jour. Sci.* **35** 90

[3] Kawazoe H, Yasukawa M, Hyodo H, Kurita M, Yanagi H and Hosono H 1997 *Nature* **389** 939

[4] Shannon R D, Rogers D B and Prewitt C T 1971 *Inorg. Chem.* **10** 713

[5] Prewitt C T, Shannon R D and Rogers D B 1971 *Inorg. Chem.* **10** 719

[6] Rogers D B, Shannon R D and Prewitt C T 1971 *Inorg. Chem.* **10** 723

[7] Daou R, Frésard R, Eyert V, Hébert S and Maignan A 2017 *Science and Technology of Advanced Materials* **18** 919

[8] Mackenzie A P 2017 *Rep. Prog. Phys.* **80** 032501

[9] Noh H J, Jeong J, Chang B, Jeong D, Moon H S, Cho E J, Ok J M, Kim J S, Kim K, Min B I, Lee H K, Kim J Y, Park B G, Kim H D and Lee S 2014 *Sci. Rep.* **4** 3680

[10] Lechermann F 2018 *Phys. Rev. Materials* **2** 085004

[11] Sunko V, Mazzola F, Kitamura S, Khim S, Kushwaha P, Clark O J, Watson M, Markovic I, Biswas D, Pourovskii L, Kim T K, Lee T L, Thakur P K, Rosner H, Moessner A G R, Oka T, Mackenzie A P and King P D C 2020 *Sci. Adv.* **6** eaaz0611

[12] Anisimov V I, Poteryaev A I, Korotin M A, Anokhin A O and Kotliar G 1997 *J. Phys.: Condens. Matter* **9** 7359

[13] Lichtenstein A I and Katsnelson M I 1998 *Phys. Rev. B* **57** 6884

[14] Kotliar G, Savrasov S Y, Haule K, Oudovenko V S, Parcollet O and Marianetti C A 2006 *Rev. Mod. Phys.* **78** 865

[15] Huda M N, Yan Y, Walsh A, Wei S H and Al-Jassim M M 2009 *Phys. Rev. B* **80** 035205

[16] Seshadri R, Felser C, Thieme K and Tremel W 1998 *Chem. Mater.* **10** 2189

[17] Sheets W C, Stample E S, Bertoni M I, Sasaki M, Marks T J, Mason T O and Poeppelmeier K R 2008 *Inorg. Chem.* **47** 2696

[18] Georges A 2004 *in Lectures on the Physics of Highly Correlated Electron Systems VIII* (AIP Conference Proceedings 715) chap 3

[19] Kotliar G, Savrasov S Y, Haule K, Oudovenko V S, Parcollet O and Marianetti C A 2006 *Rev. Mod. Phys.* **78** 865

[20] Lechermann F 2018 *in DMFT: From Infinite Dimensions to Real Materials* (Forschungszentrum Jülich GmbH) chap 6

[21] Metzner W and Vollhardt D 1989 *Phys. Rev. Lett.* **62** 324

[22] Georges A and Kotliar G 1992 *Phys. Rev. B* **45** 6479

[23] Imada M, Fujimori A and Tokura Y 1998 *Rev. Mod. Phys.* **70** 1039

[24] Georges A, Kotliar G, Krauth W and Rozenberg M J 1996 *Rev. Mod. Phys.* **68** 13

[25] Zgid D and Chan G K L 2011 *J. Chem. Phys.* **134** 094115

[26] Lin N, Marianetti C A, Millis A J and Reichman D R 2011 *Phys. Rev. Lett.* **106**(9) 096402

[27] Aryasetiawan F, Imada M, Georges A, Kotliar G, Biermann S and Lichtenstein A I 2004 *Phys. Rev. B* **70** 195104

[28] Savrasov S Y, Kotliar G and Abrahams E 2001 *Nature* **410** 793

[29] Minár J, Chioncel L, Perlov A, Ebert H, Katsnelson M I and Lichtenstein A I 2005 *Phys. Rev. B* **72** 045125

[30] Pourovskii L V, Amadon B, Biermann S and Georges A 2007 *Phys. Rev. B* **76** 235101

[31] Grieger D, Piefke C, Peil O E and Lechermann F 2012 *Phys. Rev. B* **86** 155121

[32] Lechermann F, Georges A, Poteryaev A, Biermann S, Posternak M, Yamasaki A and Andersen O K 2006 *Phys. Rev. B* **74** 125120

[33] Amadon B, Lechermann F, Georges A, Jollet F, Wehling T O and Lichtenstein A I 2008 *Phys. Rev. B* **77** 205112

[34] Potthoff M and Nolting W 1999 *Phys. Rev. B* **59** 2549

[35] Elsässer C, Takeuchi N, Ho K M, Chan C T, Braun P and Fähnle M 1990 *J. Phys.: Condens. Matter* **2** 4371

[36] Lechermann F, Welsch F, Elsässer C, Ederer C, Fähnle M, Sanchez J M and Meyer B 2002 *Phys. Rev. B* **65** 132104

[37] Meyer B, Elsässer C, Lechermann F and Fähnle M 1998 *FORTRAN 90 Program for Mixed-Basis-Pseudopotential Calculations for Crystals* Max-Planck-Institut für Metallforschung, Stuttgart

[38] Perdew J P, Burke K and Ernzerhof M 1996 *Phys. Rev. Lett.* **77** 3865

[39] Ouyang S, Li Z, Ouyang Z, Yu T, Ye J and Zou Z 2008 *J. Phys. Chem. C* **112** 3134

[40] Anisimov V I, Kondakov D E, Kozhevnikov A V, Nekrasov I A, Pchelkina Z V, Allen J W, Mo S K, Kim H D, Metcalf P, Suga S, Sekiyama A, Keller G, Leonov I, Ren X and Vollhardt D 2005 *Phys. Rev. B* **71** 125119

[41] Korotin M A, Anisimov V I, Khomskii D I and Sawatzky G A 1998 *Phys. Rev. Lett.* **80** 4305

[42] Lechermann F 2009 *Phys. Rev. Lett.* **102** 046403

[43] Rubtsov A N, Savkin V V and Lichtenstein A I 2005 *Phys. Rev. B* **72** 035122

[44] Werner P, Comanac A, de' Medici L, Troyer M and Millis A J 2006 *Phys. Rev. Lett.* **97** 076405

[45] Parcollet O, Ferrero M, Ayral T, Hafermann H, Krivenko I, Messio L and Seth P 2015 *Comput. Phys. Commun.* **196** 398

[46] Seth P, Krivenko I, Ferrero M and Parcollet O 2016 *Comput. Phys. Commun.* **200** 274

[47] Anisimov V I, Solovyev I V, Korotin M A, Czyżyk M T and Sawatzky G A 1993 *Phys. Rev. B* **48** 16929

[48] Hicks C W, Gibbs A S, Mackenzie A P, Takatsu H, Maeno Y and Yelland E A 2012 *Phys. Rev. Lett.* **109**(11) 116401

[49] Moll P J W, Kushwaha P, Nandi N, Schmidt B and Mackenzie A P 2016 *Science* **351** 1061

[50] Andreev A V, Kivelson S A and Spivak B 2011 *Phys. Rev. Lett.* **106**(25) 256804

[51] Gurzhi R 1963 *Sov. Phys. JETP* **44** 771

[52] Scaffidi T, Nandi N, Schmidt B, Mackenzie A P and Moore J E 2017 *Phys. Rev. Lett.* **118**(22) 226601

[53] Varnavides G, Jermyn A S, Anikeeva P, Felser C and Narang P 2020 *Nat. Commun.* **11** 4710

[54] Mekata M, Sugino T, Oohara A, Oohara Y and Yoshizawa H 1995 *Physica B* **213** 221

[55] Oohara Y, Mitsuda S, Yoshizawa H, Yaguchi N, Kuriyama H, Asana T and Mekata M 1994 *J. Phys. Soc. Jpn.* **63** 847

[56] Seki S, Onose Y and Tokura Y 2008 *Phys. Rev. Lett.* **101** 067204

[57] Eyert V, Frésard R and Maignan A 2008 *Chem. Mater.* **20** 2370

[58] Ong K P, Zhang J, Tse J S and Wu P 2010 *Phys. Rev. B* **81**(11) 115120

[59] Ong K P and Singh D J 2012 *Phys. Rev. B* **85** 134403

[60] Sobota J A, Kim K, Takatsu H, Hashimoto M, Mo S K, Hussain Z, Oguchi T, Shishidou T, Maeno Y, Min B I and Shen Z X 2013 *Phys. Rev. B* **88** 125109

[61] Gruner M E, Eckern U and Pentcheva R 2015 *Phys. Rev. B* **92**(23) 235140

[62] Billington D, Ernsting D, Millichamp T E, Lester C, Dugdale S B, Kersh D, Duffy J A, Giblin S R, Taylor J W, Manuel P, Khalyavin D D and Takatsu H 2015 *Sci. Rep.* **5** 12428

[63] Noh H J, Jeong J, Jeong J, Cho E J, Kim S B, Kim K, Min B I and Kim H D 2009 *Phys. Rev. Lett.* **102**(25) 256404

[64] Ok J M, Jo Y J, Kim K, Shishidou T, Choi E S, Noh H J, Oguchi T, Min B I, and Kim J S 2013 *Phys. Rev. Lett.* **111** 176405

[65] Hicks C W, Gibbs A S, Zhao L, Kushwaha P, Borrmann H, Mackenzie A P, Takatsu H, Yonezawa S, Maeno Y and Yelland E A 2015 *Phys. Rev. B* **92** 014425

[66] Lechermann F and Richter R 2020 *Phys. Rev. Research* **2** 013352

[67] Takatsu H, Yoshizawa H, Yonezawa S and Maeno Y 2009 *Phys. Rev. B* **79** 104424

[68] Mott N 1974 *Philosophical Magazine* **30** 403

[69] Doniach S 1977 *Physica B* **91** 231

[70] Bednorz J G and Müller K A 1986 *Z. Physik B - Condensed Matter* **64** 189

[71] Zubko P, Gariglio S, Gabay M, Ghosez P and Triscone J M 2011 *Annu. Rev. Condens. Matter Phys.* **2** 141

[72] Hwang H Y, Iwasa Y, Kawasaki M, Keimer B, Nagaosa N and Tokura Y 2012 *Nature Materials* **11** 103

[73] Mazin I I, Jeschke H O, Lechermann F, Lee H, Fink M, Thomale R and Valentí R 2014 *Nat. Commun.* **5** 4261

[74] Ye L, Kang M, Liu J, von Cube F, Wicker C R, Suzuki T, Jozwiak C, Bostwick A, Rotenberg E, Bell D C, Fu L, Comin R and Checkelsky J G 2018 *Nature* **555** 638

[75] Ghimire N J and Mazin I I 2020 *Nat. Mater.* **19** 137

[76] Piefke C, Boehnke L, Georges A and Lechermann F 2010 *Phys. Rev. B* **82**(16) 165118

[77] Peil O E, Georges A and Lechermann F 2011 *Phys. Rev. Lett.* **107**(23) 236404

[78] Boehnke L and Lechermann F 2012 *Phys. Rev. B* **85**(11) 115128

[79] Wallace P R 1947 *Phys. Rev.* **71**(9) 622–634

[80] Li G, Khim S, Chang C S, Fu C, Nandi N, Li F, Yang Q, Blake G R, Parkin S, Auffermann G, Sun Y, Muller D A, Mackenzie A P and Felser C 2019 *ACS Energy Lett.* **4** 2185

[81] Harada T, Fujiwara K and Tsukazaki A 2018 *APL Mater.* **6** 046107

[82] Brahlek M, Rimal G, Ok J M, Mukherjee D, Mazza A R, Lu Q, Lee H N, Ward T Z, Unocic R R, Eres G and Oh S 2019 *Phys. Rev. Materials* **3**(9) 093401

[83] Yordanov P, Sigle W, Kaya P, Gruner M E, Pentcheva R, Keimer B and Habermeier H U 2019 *Phys. Rev. Materials* **3**(8) 085403

[84] Sun J, Barone M R, Chang C S, Holtz M E, Paik H, Schubert J, Muller D A and Schlom D G 2019 *APL Mater.* **7** 121112

[85] Ok J M, Brahlek M, Choi W S, Roccapriore K M, Chisholm M F, Kim S, Sohn C, Skoropata E, Yoon S, Kim J S and Lee H N 2020 *APL Mater.* **8** 051104

[86] Wei R, Gong P, Zhao M, Tong H, Tang X, Hu L, Yang J, Song W, Zhu X and Sun Y 2020 *Adv. Funct. Mater.* **30** 2002375

[87] Harada T, Bredol P, Inoue H, Ito S, Mannhart J and Tsukazaki A 2020 *arXiv:2007.03146*

[88] Sunko V, Rosner H, Kushwaha P, Khim S, Mazzola F, Bawden L, Clark O J, Riley J M, Kasinathan D, Haverkort M W, Kim T K, Hoesch M, Fujii J, Vobornik I, Mackenzie A P and King P D C 2017 *Nature* **549** 492

[89] Mazzola F, Sunko V, Khim S, Rosner H, Kushwaha P, Clark O J, Bawden L, Marković I, Kim T K, Hoesch M, Mackenzie A P and King P D C 2018 *PNAS* **115** 12956

[90] Harada T, Sugawara K, Fujiwara K, Kitamura M, Ito S, Nojima T, Horiba K, Kumigashira H, Takahashi T, Sato T and Tsukazaki A 2020 *Phys. Rev. Research* **2**(1) 013282

[91] Sunko V, McGuinness P H, Chang C S, Zhakina E, Khim S, Dreyer C E, Konczykowski M, Borrmann H, Moll P J W, König M, Muller D A and Mackenzie A P 2020 *Phys. Rev. X* **10**(2) 021018

[92] Tanaka M, Hasegawa M and Takei H 1999 *Journal of Crystal Growth* **203** 400

[93] Kan E J, Xiang H J, Zhang Y, Lee C and Whangbo M H 2009 *Phys. Rev. B* **80**(10) 104417

[94] Arsenijević S, Ok J M, Robinson P, Ghannadzadeh S, Katsnelson M I, Kim J S, and Hussey N E 2016 *Phys. Rev. Lett.* **116** 087202

[95] Ghannadzadeh S, Licciardello S, Arsenijević S, Robinson P, Takatsu H, Katsnelson M I and Hussey N E 2017 *Nat. Commun.* **8** 15001

[96] Le M D, Jeon S, Kolesnikov A I, Voneshen D J, Gibbs A S, Kim J S, Jeong J, Noh H J, Park C, Yu J, Perring T G and Park J G 2018 *Phys. Rev. B* **98** 024429

[97] Sun D, Sokolov D A, Bartlett J M, Sannigrahi J, Khim S, Kushwaha P, Khalyavin D D, Manuel P, Gibbs A S, Takagi H, Mackenzie A P and Hicks C W 2019 *Phys. Rev. B* **100**(9) 094414

[98] Park C and Yu J 2020 *arXiv:2001.06834*

[99] Kudasov Y B 2020 *arXiv:2006.05453*

[100] Komleva E V, Irkhin V Y, Solovyev I V, Katsnelson M I and Streltsov S V 2020 *arXiv:2007.06234*